A Tale of Two Ice Shelves: Contrasting Behavior During the Regional Destabilization of the Dotson-Crosson Ice Shelf System, West Antarctica

Christian T. Wild[1,1,1], Tiago Segabinazzi Dotto[2,2,2], Karen E. Alley[3,3,3], Gabriela Collao-Barrios[4,4,4], Atsuhiro Muto[5,5,5], Rob A. Hall[2,2,2], Martin Truffer[6,6,6], Ted A. Scambos[4,4,4], Karen J. Heywood[2,2,2], and Erin C. Pettit[1,1,1]

[1]Oregon State University
[2]University of East Anglia
[3]University of Manitoba
[4]US National Snow and Ice Data Center
[5]Temple University
[6]University of Alaska Fairbanks

November 30, 2022

Abstract

The Dotson Ice Shelf has resisted acceleration and ice-front retreat despite high basal-melt rates and rapid disaggregation of the neighboring Crosson Ice Shelf. Because of this lack of acceleration, previous studies have assumed that Dotson is stable. Here we show clear evidence of Dotson's destabilization as it decelerates, contrary to the common assumption that ice-flow deceleration is synonymous with stability. Ungrounding of a series of pinning points initiated acceleration in the Upper Dotson in the early 2000s, which subsequently slowed ice flow in the Lower Dotson. Discharge from the tributary Kohler Glacier into Crosson increased, but non-proportionally. Using ICESat and ICESat-2 altimetry data we show that ungrounding of the remaining pinning points is linked to a tripling in basal melt rates between 2006-2016 and 2016-2020. Basal melt rates on Crosson doubled over the same period. The higher basal melt at Lower Dotson is consistent with the cyclonic ocean circulation in the Dotson cavity, which tends to lift isopycnals and allow warmer deep water to interact with the ice. Given current surface-lowering rates, we estimate that several remaining pinning points in the Upper Dotson will unground within one to three decades. The grounding line of Kohler Glacier will retreat past a bathymetric saddle by the late 2030s and merge into the Smith West Glacier catchment, raising concern that reconfiguration of regional ice-flow dynamics and new pathways for the intrusion of warm modified Circumpolar Deep Water could further accelerate grounding-line retreat in the Dotson-Crosson Ice Shelf System.

Hosted file

`dis_2d_2020_animation.gif` available at https://authorea.com/users/464602/articles/609012-a-tale-of-two-ice-shelves-contrasting-behavior-during-the-regional-destabilization-of-the-dotson-crosson-ice-shelf-system-west-antarctica

A Tale of Two Ice Shelves: Contrasting Behavior During the Regional Destabilization of the Dotson-Crosson Ice Shelf System, West Antarctica

Christian T. Wild[1]*, Tiago S. Dotto[2], Karen E. Alley[3], Gabriela Collao-Barrios[4], Atsuhiro Muto[5], Rob A. Hall[2], Martin Truffer[6], Ted A. Scambos[4], Karen J. Heywood[2] and Erin C. Pettit[1]

[1]College of Earth, Ocean, and Atmospheric Sciences, Oregon State University, Corvallis OR, USA
[2]Centre for Ocean and Atmospheric Sciences, School of Environmental Sciences, University of East Anglia, Norwich, NR4 7TJ, UK
[3]Department of Environment and Geography, University of Manitoba, Winnipeg, Manitoba, CAN
[4]National Snow and Ice Data Center, University of Colorado Boulder, Boulder CO, USA
[5]Department of Earth and Environmental Science, Temple University, Philadelphia PA, USA
[6]Geophysical Institute and Department of Physics, University of Alaska Fairbanks, Fairbanks AK, USA

Key Points:

- Both the Dotson and Crosson Ice shelves are destabilizing, despite ice-flow deceleration and the appearance of a new pinning point
- Ungrounding of the remaining pinning points is linked to an increase of ocean forcing, which is in accordance with warm mCDW pathways
- Asymmetric retreat of the grounding line will soon allow research of the processes that drive regional destabilization in the Amundsen Sea

*Current address, College of Earth, Ocean, and Atmospheric Sciences, OR 97331, 104 CEOAS Admin Building

Corresponding author: Christian T. Wild, `wildch@oregonstate.edu`

Abstract

The Dotson Ice Shelf has resisted acceleration and ice-front retreat despite high basal-melt rates and rapid disaggregation of the neighboring Crosson Ice Shelf. Because of this lack of acceleration, previous studies have assumed that Dotson is stable. Here we show clear evidence of Dotson's destabilization as it decelerates, contrary to the common assumption that ice-flow deceleration is synonymous with stability. Ungrounding of a series of pinning points initiated acceleration in the Upper Dotson in the early 2000s, which subsequently slowed ice flow in the Lower Dotson. Discharge from the tributary Kohler Glacier into Crosson increased, but non-proportionally. Using ICESat and ICESat-2 altimetry data we show that ungrounding of the remaining pinning points is linked to a tripling in basal melt rates between 2006-2016 and 2016-2020. Basal melt rates on Crosson doubled over the same period. The higher basal melt at Lower Dotson is consistent with the cyclonic ocean circulation in the Dotson cavity, which tends to lift isopycnals and allow warmer deep water to interact with the ice. Given current surface-lowering rates, we estimate that several remaining pinning points in the Upper Dotson will unground within one to three decades. The grounding line of Kohler Glacier will retreat past a bathymetric saddle by the late 2030s and merge into the Smith West Glacier catchment, raising concern that reconfiguration of regional ice-flow dynamics and new pathways for the intrusion of warm modified Circumpolar Deep Water could further accelerate grounding-line retreat in the Dotson-Crosson Ice Shelf System.

Plain Language Summary

Ice shelves, the floating extensions of the Antarctic Ice Sheets, are a key factor in stabilizing their tributary glaciers. As ice shelves are pushed against islands and scratch over submerged mountain tops at their base, they build up pressure that significantly slows down glacier discharge into the ocean. Changes in ice shelves are therefore an early-warning system for future variations in sea-level rise. The paper shows that the slow-down of an ice shelf does not necessarily imply increased stability, contrary to common belief. Ice piracy by a rapidly accelerating, adjacent glacier reduced ice inflow to the ice shelf causing widespread deceleration. Furthermore, warmer ocean waters that circulate in the cavity caused a rapid increase in melting underneath the ice shelf. Basal melting will soon lead to unpinning of the ice base from a series of highs on the seafloor. Unpinning thereafter will not only further destabilize the ice shelf but is also threatening to open up new pathways for the intrusion of warm ocean water deep underneath the West Antarctic Ice Sheet.

1 Introduction

Antarctic mass loss rates are currently the highest in glaciers draining into the Amundsen Sea (Smith et al., 2020). The Dotson Ice Shelf lies along the Walgreen Coast and is fed by branches of Smith West and Kohler Glacier (Fig. 1). It is confined by Bear Island to the east and Martin Peninsula to the west, and it features a well-defined shear margin with the adjacent and much faster flowing Crosson Ice shelf. The drainage basins of the Dotson (17 400 km^2) and the Crosson (12 800 km^2) have a combined potential of raising global sea level by 6 cm (Rignot et al., 2019). Although this potential is relatively small compared with 51 and 65 cm of the vast drainage basins of Pine Island (181 400 km^2) and Thwaites Glacier (192 800 km^2), respectively, the Dotson-Crosson Ice Shelf system contributes one fourth of the contemporary total mass loss in the Amundsen Sea (Rignot et al., 2019; Milillo et al., 2022). Numerical model simulations of its future evolution indicate that thinning of its tributary glaciers could reach the ice divide separating the Dotson-Crosson Ice Shelf system from the Thwaites Glacier catchment as quickly as thinning initiated at Thwaites Glacier's grounding line (Lilien et al., 2019).

While the Crosson, fed by the rapidly retreating Pope and Smith Glaciers, almost doubled in speed since the late 1970s, large parts of the Dotson maintained near-constant velocity, which was attributed to the sustained competency of the ice shelf (Lilien et al., 2018). Although there is no reported evidence of flow acceleration through the 1970s and 1980s (Lucchitta et al., 1994), the ice surface of the Dotson lowered at a rate of 2.6 m/yr between 1994 and 2012 (Paolo et al., 2015), which was likely triggered by an increase in the incursion of warm modified Circumpolar Deep Water (mCDW) in the mid-/late-2000s (Jenkins et al., 2018). Thinning caused the ungrounding of many ice-shelf pinning points (Scheuchl et al., 2016) and induced acceleration of the tributary Kohler Glacier (Mouginot et al., 2014), where some of Antarctica's most rapid basal melting of 40 to 70 m/yr has been measured from airborne observations (Khazendar et al., 2016). Average basal melt rates were estimated to be 7.8 $\pm$ 0.6 m/yr and 11.9 $\pm$ 1.0 m/yr between 2003 to 2008 on the Dotson and Crosson, respectively (Rignot et al., 2013). More recently, a single, wide basal channel has formed, featuring sustained surface lowering from its origin in the Upper Dotson up to the ice shelf's calving front about 60 km downstream (Gourmelen et al., 2017).

The grounding zone of Kohler Glacier, which feeds mostly into the Lower Dotson (Fig. 1b and Fig. 3), has a complex history. The grounding zone readvanced between 2011 and 2014 following nearly a decade of grounding-line retreat since 1992 (Fig. 1a, Scheuchl et al., 2016). This was followed by a retreat of 2.3 $\pm$ 0.4 km between 2016 and 2018 to an almost stagnant grounding-line location between 2018 and 2020, where bedrock slopes remain prograde for another 2 km upstream to where upper Kohler Glacier splits into lower Kohler Glacier and Smith West Glacier (Fig. 1c, Milillo et al., 2022). Extrapolating Kohler Glacier's grounding-line retreat rate of 0.5 km/yr between 2016 to 2020 suggests that the two glaciers will merge entirely within the next 15 years (Milillo et al., 2022). In light of this imminent reorganization of ice-flow dynamics, it is important to understand the current state of the Dotson-Crosson Ice Shelf System and to predict both regional grounding-line-retreat patterns and future pathways of mCDW intrusion.

In this paper we integrate ICESat and more recent ICESat-2 measurements of surface elevation with numerical modeling of tidal ice-shelf flexure to derive height above flotation and surface-lowering rates over the entire Dotson-Crosson Ice Shelf System. This is necessary to assess the stability of the remaining ice-shelf pinning points as well as to predict future grounding-line retreat of the tributary Pope, Smith and Kohler Glaciers. We validate our results with independent measurements of recent grounding-line positions from InSAR (Milillo, 2021) and estimate uncertainty with available field data collected in January 2020 as part of the NERC/NSF International Thwaites Glacier Collaboration's Thwaites-Amundsen Regional Survey and Network Integrating Atmosphere-Ice-Ocean Processes (TARSAN) project. After reviewing past changes in observed ice dynamics, we show how height above flotation can be used to interpret the contemporary structural integrity of ice-shelf pinning points. We then calculate surface-lowering rates in comparison with the high-resolution REMA digital elevation model to unveil a rapid increase in basal melt rates underneath the floating ice shelves, which is likely due to enhanced and southward migration of the polar westerlies pushing warm Circumpolar Deep Water towards the Antarctic coastline (e.g., Wåhlin et al., 2013; Holland et al., 2019; Dotto et al., 2020). After discussing our results in light of new, ship-based, measurements of water circulation along the Dotson's front, we explore the consequences of sustained current surface-lowering rates for the grounded parts to assess the timing of grounding line retreat at Kohler Glacier as it will be absorbed into the catchment of Smith West Glacier. Our results also provide guidance for future research focus in this critical region of West Antarctica.

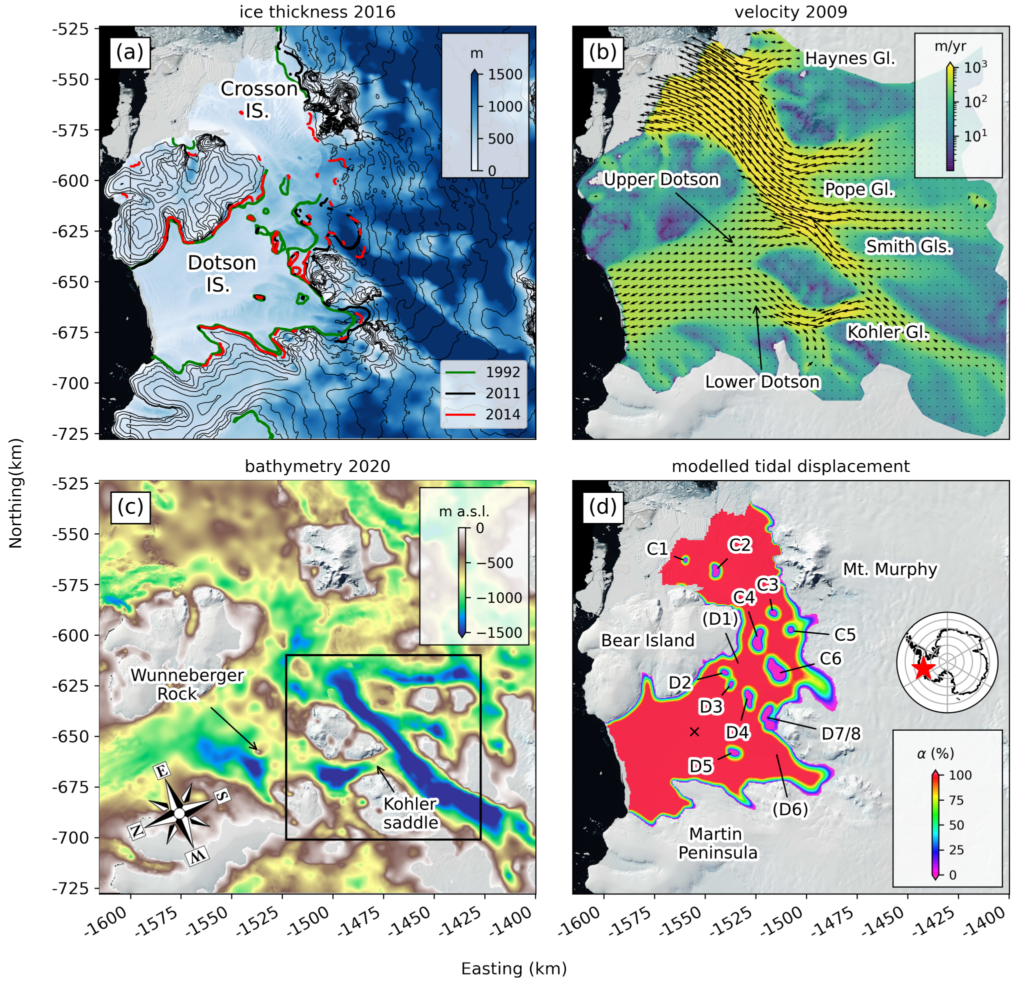

Figure 1. Data sets assembled for the Dotson-Crosson Ice-shelf system overlain on the Landsat Image Mosaic of Antarctica (Bindschadler et al., 2008): (a) BedMachine version 2 ice thickness (Morlighem, 2020). Past grounding lines are from NASA's Making Earth System Data Records for Use in Research Environments (MEaSUREs, Rignot et al., 2017). Black lines correspond to 100 m contours of surface elevation. (b) The MEaSUREs Antarctic-wide ice surface velocity product from InSAR data acquired in 2009 from which we derive strain rates. (c) BedMachine version 2 bathymetry/bed topography (Morlighem, 2020) in meters above sea level. (d) Modeled percentage tidal displacement as calculated using an elastic finite-element model showing (red) freely-floating areas synchronous with the tidal oscillation and (purple) completely grounded areas outside the reach of vertical tidal forcing. The black cross shows the location where tides were modeled using CATS2008 (Padman et al., 2002, 2008). The black rectangle in panel c shows the spatial extent of Figure 12a. The red star in the inset in panel (d) marks the location in the Amundsen Sea Embayment in West Antarctica. Labels highlight the location of features discussed in the main text. Coordinates in Antarctic Polar Stereographic projection (EPSG:3031).

2 Data and methods

2.1 Velocity and ice thickness data

We use mosaics of ice motion in the Amundsen Sea Embayment from the NASA Making Earth System Data Records for Use in Research Environments (MEaSUREs) Program, Version 1 (Rignot et al., 2014), which were assembled from interferometric synthetic-aperture radar (InSAR) data acquired in 1996, 2000, 2002, and 2006-2012 by multiple satellites as well as the Antarctic-wide MEaSUREs InSAR-Based Antarctica Ice Velocity product, Version 2, extending the record to 2016 (Rignot et al., 2017). Velocity data between 1985 and 2018 were derived from Landsat 4, 5, 7, and 8 imagery using the auto-RIFT feature tacking processing chain (Gardner et al., 2018) and provided by the NASA Inter-mission Time Series of Land Ice Velocity and Elevation (ITS_LIVE) project (Gardner et al., 2019). Unless stated otherwise, we use the BedMachine Antarctica, Version 2 ice thickness product (Morlighem, 2020), which was derived via mass conservation, streamline diffusion, and other methods (Morlighem et al., 2020).

2.2 Surface elevation data

The Reference Elevation Model of Antarctica (REMA, Howat et al., 2019) was mosaiced from a series of 2 m-resolution DEM strips derived from GeoEye and Worldview satellite imagery spanning 2012 to 2016 and vertically registered to Cryosat-2 altimetry data. To detect ice-surface elevation change between 2003 and 2016, we differenced migrated ICESat data from the regional Level-2 GLAH12 release 634 global altimetry data (Zwally et al., 2014) with the REMA mosaic. Additionally we only retained measurements unaffected by clouds. ICESat-2 data were provided as part of the ATL06 land-ice data release, Version 3 (Smith et al., 2019). We removed 9.8% of the ICESat-2 points with the provided quality summary flag. ICESat-2 data were acquired between 2018 to 2020 and allow us to calculate surface elevation changes between 2016 and 2018/20 when differenced from REMA.

2.3 Tidal corrections

Freely-floating ice shelves are subject to tidal oscillations as well as elastic deformation of the Earth's crust underneath the weight of the moving water masses. We use the regional barotropic Circum-Antarctic Tidal Solution (CATS2008) model developed by Padman et al. (2002, 2008) and the fully global barotropic assimilation model (TPXO9) from Oregon State University developed by Egbert and Erofeeva (2002) to predict ocean tides and tidal loading at a point in the center of the Dotson (-112.6073° W, -74.5842° S, black cross in Fig. 1d) and then use these values to apply across the whole ice shelf. An offshore location on its freely-floating part is chosen, as any tide model may be inaccurate in the vicinity of grounded features. Additionally, we correct for the inverse barometric effect (Padman et al., 2003) using an atmospheric pressure record obtained by an automatic weather station on nearby Thurston Island.

Regions of the ice shelf near the grounding line or pinning points are affected by tides, but they are not entirely freely floating. To account for tides at these locations, we calculate the magnitude of tidal flexure. We approximate tidal flexure with the well-known elastic formulation (Walker et al., 2013):

$$
\begin{aligned}
k\mathbf{w} + \nabla^2\left(\mathbf{D}\nabla^2\mathbf{w}\right) &= \mathbf{q}, \\
\mathbf{D} &= \tfrac{E\mathbf{H}^3}{12(1-\lambda^2)}, \\
\mathbf{q} &= \rho_{sw} g\left(A - \mathbf{w}\right),
\end{aligned} \tag{1}
$$

where $\mathbf{w}$ is the vertical deflection field, ∇^2 the 2D Laplacian and $k = 5$ MPa/m a spring constant of the foundation which is zero for the floating part. $\mathbf{D}$ is the vertically integrated ice-shelf stiffness field (Love, 1906, p. 443) with $E = 1.5$ GPa the effective Young's modulus, $\mathbf{H}$ is ice thickness given by BedMachine and $\lambda = 0.4$ is Poisson's ratio of a Maxwell rheological model (Gudmundsson, 2011). The tidal force field underneath the floating ice, $\mathbf{q}$, is given by the tidal amplitude $A = 1$ m, the density of ocean water $\rho_{sw} = 1027$ kg/m^3 and gravitational acceleration $g = 9.81$ m/s^2. We define a grounding-line fulcrum ($\mathbf{w} = 0$) and rigidly anchor the upstream boundaries of the computational domain to a tributary ice stream ($\mathbf{w} = 0$, $\nabla^2\mathbf{w} = 0$). The finite-element model is solved in COMSOL Multiphysics (Suppl. video) and has been applied in several related studies to correct surface elevation measurements for tidal flexure (e.g., Alley et al., 2021; Wild et al., 2022). Lastly, we normalize the model solutions for $\mathbf{w}$ with the applied tidal amplitude A to derive a field of tide-deflection ratio (α map, Han and Lee (2014), Fig. 1d) and directly scale the tide model output to include the effects of tidal flexure where ice is not freely floating. We apply this type of tide correction to ICESat and ICESat-2 data to derive surface-lowering rates from which we later calculate basal-melt rates underneath the floating ice.

2.4 Height above flotation calculation

We first invert freeboard to corresponding flotation ice thickness, $\mathbf{H_f}$, by assuming the EIGEN6c4 geoid model (Förste et al., 2014) as the mean sea level. We use field data from January 2020 to calculate a mean ice column density of $\rho = 890 \pm 5$ kg/m^3 from 16 sites distributed across the Upper Dotson (Fig. 11a). At each site we derived freeboard from static GPS measurements of surface elevation and phase-sensitive radar measurements of local ice thickness. We compare these in-situ values to remotely-sensed freeboard at each site using ice-surface elevations from REMA and ice-thickness from BedMachine (Fig. 1a) from which we derive $\rho = 886 \pm 20$ kg/m^3. Height above flotation, $\mathbf{z_f}$, is then calculated as the difference between flotation ice thickness and absolute ice thickness, $\mathbf{H_a}$, from BedMachine:

$$\mathbf{z_f} = (\mathbf{H_f} - \mathbf{H_a}) * (\frac{\rho_{sw} - \rho}{\rho_{sw}}), \tag{2}$$

Where $\rho_{sw} = 1027$ kg/m^3 is the density of seawater. We then use height above flotation to delineate a grounding-line, which agrees well with an InSAR-derived grounding-line product (Fig. 5, Milillo, 2021) . Some of the differences between the InSAR-derived grounding line and our product derived from height above flotation are due to the differing time period of data collection. The degree of grounding of individual ice-shelf pinning points, where InSAR-derived grounding lines are not available, is determined from their absolute height above flotation.

2.5 Basal melt rate from mass conservation

Surface-elevation measurements are usually taken in an Eulerian reference frame, which is fixed in space and time relative to the geoid. Signals of surface-elevation change are introduced as new surface features advect, particularly in fast-flowing areas such as ice shelves and outlet glaciers. We therefore choose a Lagrangian reference frame to calculate surface-elevation change and track ice parcels as they advect with the ice flow. Lagrangian analysis has become the standard procedure for change detection in areas with rough surface and significant advection (Dutrieux et al., 2013; Moholdt et al., 2014; Shean et al., 2017, 2019; Berger et al., 2017; Alley et al., 2021; Wild et al., 2022). To track movement along trajectories, we use the ITS_LIVE record to migrate ICESat data forwards and ICESat-2 data backwards in time to locations where each altimetry point would have been during the acquisition of REMA. A sufficiently small timestep is thereby critical to limit horizontal migration of the altimetry points to the 40-m spatial resolution of the ITS_LIVE velocity grid, also known as the Courant-Friedrichs-Lewy condition. We choose a 7.3 day temporal resolution, guided by the maximum flow velocity of 4.31 m/d (1575 m/yr) within our domain. We then smooth the tide-corrected ICESat and ICESat-2 elevation measurements along-track using a moving average of five altimetry points and subtract the earlier elevation measurement from the later time at migrated altimetry point locations. Lastly, we rasterize the migrated point cloud using a 2D Gaussian Kernel to obtain maps of surface-lowering rates in relation to 2016 when REMA data were acquired. Our derived surface lowering rates are valid on both grounded and floating ice and can be used to monitor thinning of grounded tributary glaciers as well as the derivation of basal melt rates underneath freely-floating areas using mass conservation principles.

Basal-melt rates, $\dot{\mathbf{m}}_{\mathbf{b}}$, are calculated from Lagrangian ice-thickness change, $\frac{\mathrm{D}\mathbf{H}}{\mathrm{D}t}$, the dynamic-thickness change and the surface mass balance using the depth-integrated continuity equation (Jenkins & Doake, 1991):

$$\frac{\mathrm{D}\mathbf{H}}{\mathrm{D}t} + \mathbf{H}(\dot{\epsilon}_{\mathbf{lon}} + \dot{\epsilon}_{\mathbf{trans}}) = \dot{\mathbf{m}}_{\mathbf{s}} + \dot{\mathbf{m}}_{\mathbf{b}}, \tag{3}$$

For surface mass balance, $\dot{\mathbf{m}}_{\mathbf{s}}$, we use the 5.5 km resolution 1979 to 2015 average from the Regional Atmospheric Climate MOdel (RACMO) version 2.3 (Lenaerts et al., 2018), converted to ice equivalent (positive for accumulation, negative for ablation). Average accumulation on the floating parts is about 1±0.3 m/yr. Dynamic thickness change (positive for divergence, negative for convergence) is derived from longitudinal, $\dot{\epsilon}_{\mathbf{lon}}$, and transverse strain rate fields, $\dot{\epsilon}_{\mathbf{trans}}$, based on the MEaSUREs velocity field that represents a longer term state (Fig. S1). We use a logarithmic strain rate formulation (Alley et al., 2018) at a length scale of four times the local ice thickness. In the absence of basal friction a constant vertical velocity profile is assumed throughout the floating ice shelf. As both the ice thickness changes and the calculation of basal melt rates (positive for freezing, negative for melting) assume hydrostatic equilibrium, we use our α map and mask out areas of tidal ice-shelf flexure before and after the point migration (Fig. 1d).

2.6 Evaluation with in-situ data

Accurate velocity fields are crucial for calculating reliable basal melt rates, particularly because Lagragian ice thickness change is the dominant term in Eq. 3 with both dynamic thickness change and surface mass balance about one magnitude smaller across the majority of both ice shelves. We therefore validate the ITS_LIVE record with available GPS measurements from January 2020. GPS data were processed using the baseline processing tool track, which is part of the GAMIT/GLOBK GPS processing software (ver. 10.71, http://geoweb.mit.edu/gg/; Chen, 1999). The data were processed kinematically against a fixed base station at Backer Island (accessed through UNAVCO, www.unavco.org, April 2020), and converted into Antarctic Polar Stereographic coordinates (EPSG: 3031) using pyproj 4 (https://pypi.org/project/pyproj/) from which velocities were calculated. Errors are estimated to be below 0.01 m, based on the standard deviation of the point cloud resulting from the kinematic processing. The resulting ice-flow-speed deviations are -0.9 ± 13 m/yr in mean and standard deviation, with a directional bias of 4±6 degree (Fig. 2a and b). Given these error bounds and the 10 years between ICESat and REMA, altimetry points can be migrated to be within an elliptical area of 541 m^2 with a 98.9% confidence. The average 3 years between REMA to ICESat-2 results in a smaller ellipse of 193 m^2 (Appendix A). These correspond to 2 and 1 grid cells in the Easting direction for ICESat and ICESat-2, respectively, and are mostly a result of ice-flow-speed deviations. The smaller directional inaccuracies keep points within the migrated grid cells in the Northing direction. We are therefore confident in detecting Lagragian surface-elevation change for features larger than about 100 m length scale, such as most ice-shelf pinning points and basal channels.

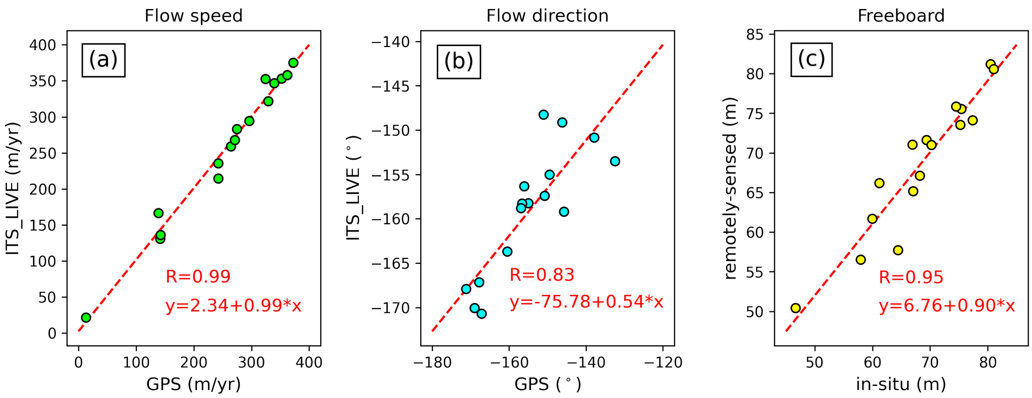

Figure 2. Validation of satellite observations with field measurements collected in Jan 2020: (a) ice-flow speed and (b) direction from Easting between ITS_LIVE 2018 and GPS, (c) comparison of in-situ derived freeboard from GPS measurements of ice-shelf surface elevation and phase-sensitive measurements of ice-column thickness with remotely-sensed freeboard from REMA and BedMachine at 16 sites distributed across the Upper Dotson (Fig. 11).

Lagragian ice-thickness change also depends on ice-surface elevation and firn depth, which reduces the mean density of the ice column and thus impacts the freeboard conversion through reduction of ice density. We compare in-situ measured freeboard at 16 sites with remotely-sensed freeboard and find deviations of -0.2 ± 2.9 m, corresponding to 1.8±27 m ice thickness in hydrostatic equilibrium. With a mean ice-shelf thickness of 468 m, the maximum estimate of ice-shelf thickness deviation is still only around 6%. With the basal channel on Dotson accounting for 30% of the total ice thickness change (Gourmelen et al., 2017), we are confident in reliably detecting regional variations in ice-shelf thinning and ultimately identify focused areas of increased basal-melt rates from the analysis of remote-sensing data.

Height above flotation is calculated from ICESat-2 data in an Eulerian reference frame and is therefore independent of uncertainties in the velocity field. However, acquisition of these altimetry measurements does not coincide with the utilized BedMachine ice-thickness product, which is a combination of several Operation IceBridge missions between 2009 and 2019. To estimate the combined effect of thinning and ice advection signals, we use the BedMachine ice-thickness error map. Area-wide error for the Dotson-Crosson Ice-Shelf System is 119.8 m and 44.2 m excluding floating ice shelves (Appendix C). For an approximate time span of 10 years between acquisition of airborne radar measurements and ICESat-2 data, the total uncertainty of height above flotation is $\sigma z_f = 19.9$ m a.f. and 4.4 m a.f., respectively. This fits well with the uncertainty estimates derived from error propagation of $\sigma z_f = 16.5$ m a.f. and 6.1 m a.f. earlier.

2.7 Oceanographic dataset

Ocean currents along the front of Dotson Ice Shelf were measured at 24 stations with an upward- and downward-looking RDI Workhorse 300-kHz Lowered Acoustic Doppler Current Profiler (LADCP) system installed on a Conductivity, Temperature and Depth (CTD) rosette onboard the RVIB Nathaniel B. Palmer between January 21 and February 7, 2022. The LADCP data were processed using the LDEO-IX toolbox (Thurnherr, 2018) and constrained by CTD/GPS and 38-kHz ship-mounted ADCP data. The barotropic tidal component of the flow was removed using the CATS2008 tidal model (Padman et al., 2002, 2008) for the time and location of each profile. Conservative temperature was calculated using the TEOS-10 toolbox (McDougall & Barker, 2011). All profiles were visually inspected and spurious data were removed.

3 Results

3.1 Changes in ice dynamics

According to the MEaSUREs Antarctic-wide velocity mosaic, mean ice-flow speed on the Dotson is 278 ± 132 m/yr with a local maximum near the inflow of the Kohler Glacier of 814 m/yr. The Crosson flows about 3 times faster at 890±265 m/yr and reaches up to 1575 m/yr near the ice-shelf front (Fig. 1b). The annual velocity record shows significant regional variations in ice-flow-speed changes since 1992 (Fig. 3). While most areas of the Dotson accelerated in the 2000s (Fig. 3a), only the Upper Dotson continued its acceleration into the 2010s. The Lower Dotson decelerated even beyond the grounding line of Kohler Glacier since 2009 (Fig. 3b). While this flow deceleration is still ongoing in 2018 (Fig. 3d), the flow acceleration in the Upper Dotson has reversed its sign in the mid 2010s and is now also decelerating in 2018 (Fig. 3b).

The velocity record also indicates that ice-flow speeds in the upper branches of Smith West and East Glaciers, as well as Kohler Glacier, have not yet peaked and are continuously accelerating as they adjust to the weakening of Crosson (Fig. 3 c and d). Although ice-flow acceleration of Pope Glacier slowed down from an increase of $>$ 100 m/yr to $<$ 100 m/yr between the 2000s and 2010s, both branches of Smith Glacier and the upstream parts of Kohler Glacier are speeding up from about 300 m/yr to $>$ 350 m/yr (Fig. 3a and b). While both branches of Smith Glacier were speeding up in a similar range, the much deeper ice-bed topography underneath Smith West Glacier caused its ice discharge to surpass Smith East Glacier (Fig. 4). Grounding-line flux of Smith West Glacier quadrupled to 19.4 Gt/yr in 2018, doubled for Smith East Glacier to 13.5 Gt/yr, with both on a continuing trend throughout the record. Deceleration of the Lower Dotson caused a reduction in grounding-line flux of Kohler Glacier from a peak of 7 Gt/yr in 2013 to 6.6 Gt/yr in 2018. Pope Glacier's discharge has stagnated since the early 2000s around 5.9 Gt/yr after a jump from 4.4 Gt/yr in 1992.

3.2 Pinning-point stability and grounding-line retreat

We validate our height-above-flotation calculation with the independent grounding-line dataset from Milillo (2021) and find approximate agreement between the datasets (Fig. 5). Although delineating grounding lines from height above flotation is less accurate than mapping from double-differential InSAR (Brunt et al., 2010), they can be used to fill gaps in SAR data acquisition, which ultimately refines grounding-line-retreat rates (Wild et al., 2022). Here, ICESat-2 data for our height-above-flotation calculation were collected between 2018 to 2020 and are overlapped by the dedicated COSMO-SkyMed constellation to survey the Amundsen Sea Embayment since 2014. Comparing the height above flotation to the recently delineated grounding lines from InSAR confirms the rapid glacier retreat reported in Milillo et al. (2022, Fig. 5). InSAR-derived grounding lines, however, tend to be a few hundred meters further inland than the transition between floating ($z_f = 0$ m a.f.) and grounded areas ($z_f > 0$ m a.f.). We attribute this either to double-differential InSAR being sensitive to the farthest inland displacement during the single epochs of SAR image acquisition, or because InSAR rather delineates the location of a 'hinge' line and not the true grounding line, where the ice base detaches from the bed and ice shelves become afloat (Fricker et al., 2009). The combined uncertainty of the derived height above flotation is a result from errors in the ICESat-2 data, BedMachine and its spread to in-situ measurements of ice-shelf freeboard in combination with errors in mean ice-column density. Calculations of error propagation yield a combined uncertainty $\sigma z_f = 16.5$ m a.f. as our upper-limit estimate, whereas the true uncertainty

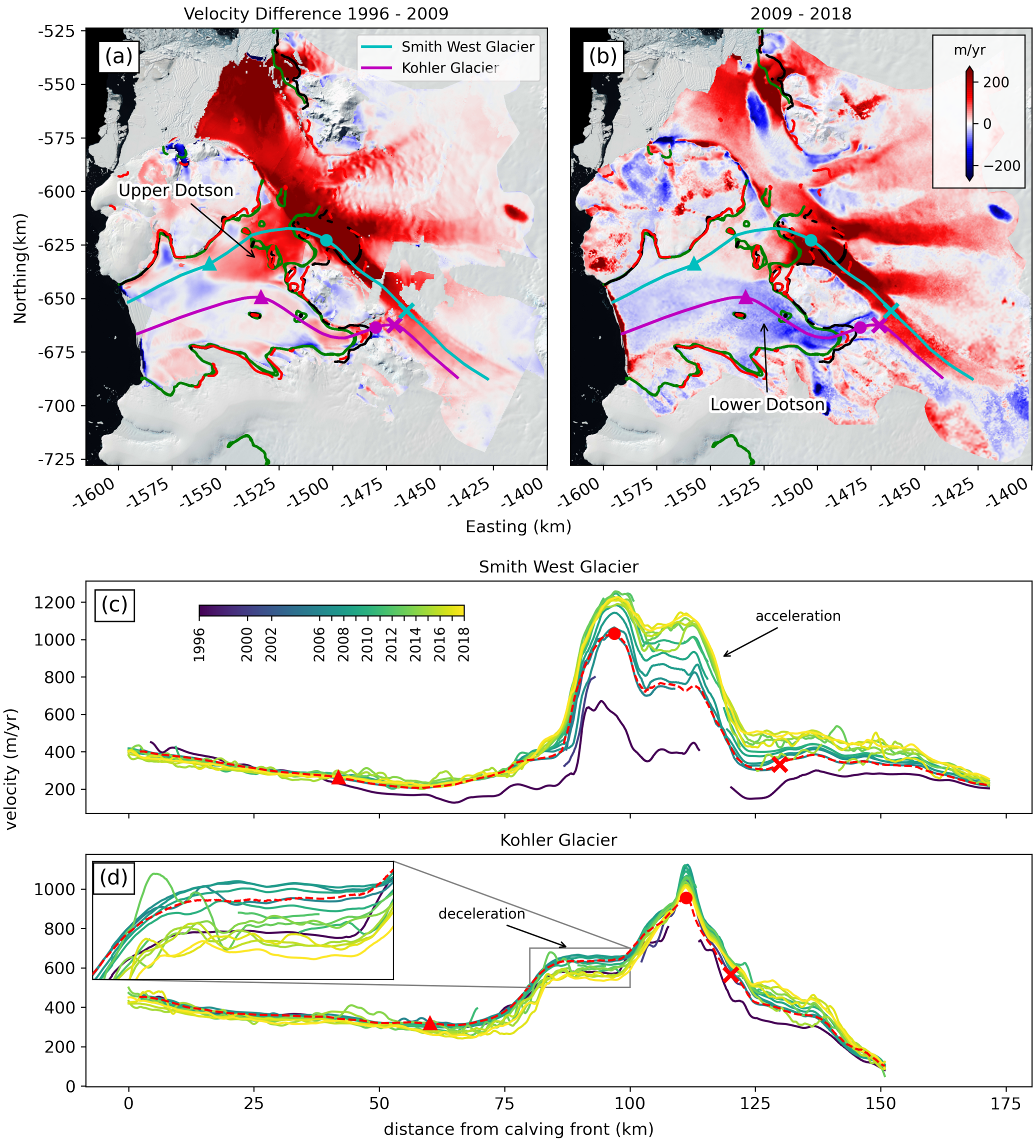

Figure 3. Changes in velocity from the MEaSUREs Antarctic-wide velocity mosaic over the past two decades : (a) Acceleration of the Upper Dotson between 1996 and 2009, and (b) deceleration of the Lower Dotson between 2009 and 2018. (c) Velocity evolution along streamlines from Smith Glacier's Western branch feeding into the Upper Dotson. Note the continued flow acceleration in the upper branch of Smith West Glacier. (d) Kohler Glacier feeding into the Lower Dotson. The inset in panel (d) highlights the flow deceleration in the Lower Dotson. Note the reversal from deceleration to acceleration about 100 and 120 km from the calving front for Smith West and Kohler Glacier, respectively, indicating that marine ice-sheet instability may be at play in this area. Transects along the flowlines in panels a and b are shown in Fig. 7a and b, respectively. Crosses indicate the location where Kohler Glacier separates from Smith West Glacier to drain into the Lower Dotson. Circles show the location of the maximum ice speed along the flowlines and triangles identify the location of downstream changes in ice dynamics such as acceleration of the Upper Dotson and deceleration of the Lower Dotson.

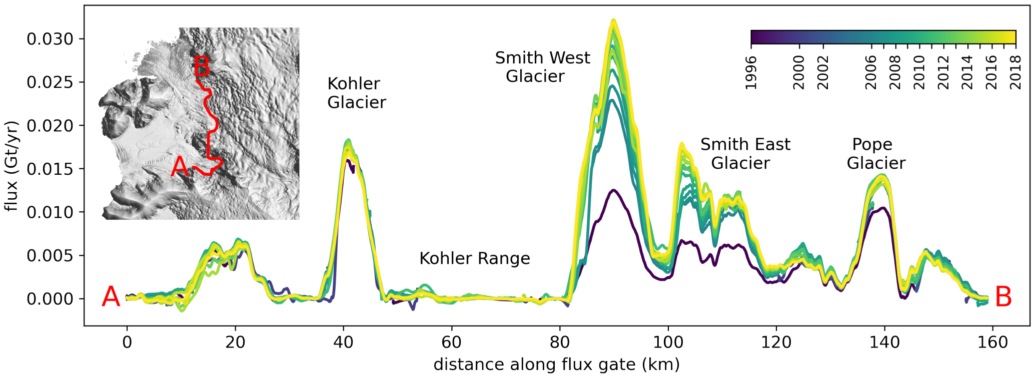

Figure 4. Ice-flux across the A-B flux gate between 1996 and 2018. Note the decrease in the discharge of Kohler Glacier, while discharge of Smith West and East Glaciers accelerated. Discharge of Pope Glacier is nearly steady. Negative values are caused by floating ice regrounding along seaward protrusions of the grounding line/flux gate.

of height above flotation is much more likely to be around $\sigma z_f = 6.1$ m a.f., because we are mainly interested in grounded areas excluding floating ice shelves (Appendix C).

Freely floating areas of ice shelves generally feature a zero height above flotation if no other stresses are present. Positive values indicate either the degree of grounding or can be used as a proxy for assessing the present stress configuration within the ice shelf. Mapping of recent height above flotation from ICESat-2 data shows that large parts of the Dotson-Crosson Ice-Shelf System are in local hydrostatic equilibrium with the ocean (Fig. 6a).

The Upper Dotson was anchored by 4 individual pinning points, which were visible in interferometric fringes in 1996 (labeled D1-4 in Scheuchl et al., 2016, and Fig. 1d). D1 ungrounded in the late 1990s, its remaining ice bulge slowly advected downstream and headed towards D2 (Suppl. video). D3 ungrounded in 2014 following years of progressive unpinning. With their extent continuously reducing, only D2 and D4 currently feature visible surface crevassing (Fig. 6b and Suppl. photos). This is because of vertical shearing induced by ice-shelf regrounding on bathymetric highs. Zero height above flotation confirms that the previously reported, ungrounded pinning points D1 and D3 provide no resistance to the ice flow. Only D4 and the much smaller D2 pinning point are currently grounded up to 46 and 26 m above their flotation level, respectively, indicating that D4 will outlive D2 with continued ice-shelf thinning.

The Lower Dotson was anchored by the two pinning points D5 and D6. While D5 penetrates through the ice-shelf surface to form the prominent Wunneberger Rock (Suppl. photos), longitudinal stresses within the ice force the upstream ice shelf far above its flotation level (Fig. 6c). D6 ungrounded entirely in the early 2010s after a period of ephemeral re-grounding during low tides in 2014 (Scheuchl et al., 2016). Our analysis confirms that the Lower Dotson has now completely detached from D6 (Figs. 6a and 7b). D7 and D8, formed on the flanks of the Kohler Range, are grounded up to 17 and 38 m a.f., respectively.

The Crosson featured 5 pinning points (labeled C1-5 in Fig. 1 d). While C1 and C3 were already ungrounded in 2014, C2 was still showing signs of grounding until 2015 (Scheuchl et al., 2016). Our height above flotation analysis shows that C2 has since ungrounded and is now an area of significant rifting. Currently, C4 shows active surface

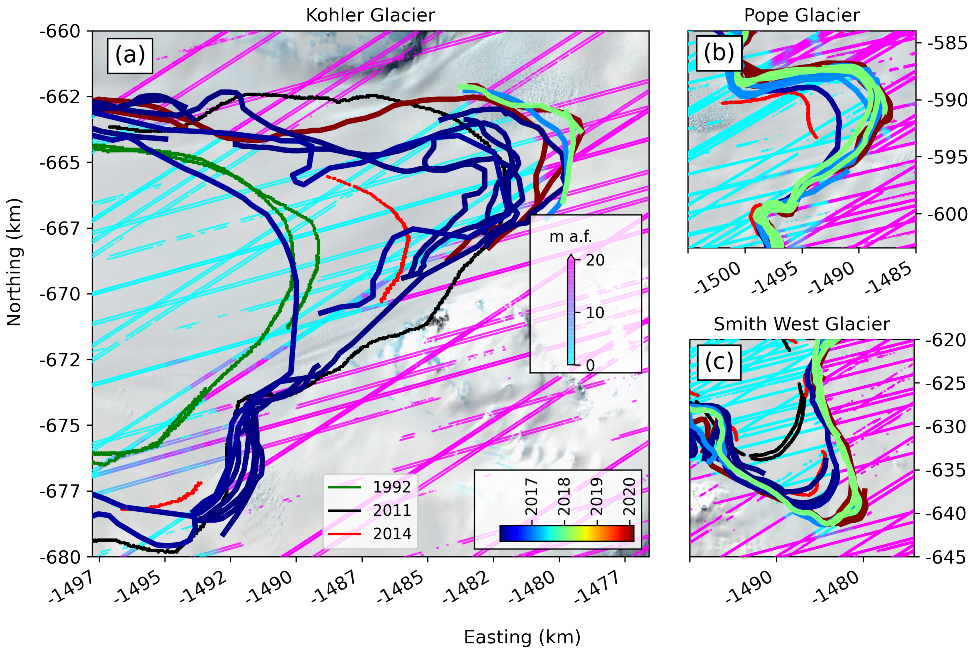

Figure 5. Comparison of grounding-line retreat of tributary glaciers derived from height above flotation and InSAR (Milillo, 2021): (a) Kohler Glacier draining into the Lower Dotson, (b) Pope Glacier draining into the Crosson and (c) Smith West Glacier draining into the Upper Dotson. Note the retreat and re-advance of Kohler Glacier between 1992/2011 and 2011/14, and the excellent fit to the InSAR-derived grounding lines between 2018/20 when ICESat-2 data were acquired for the height above flotation calculation.

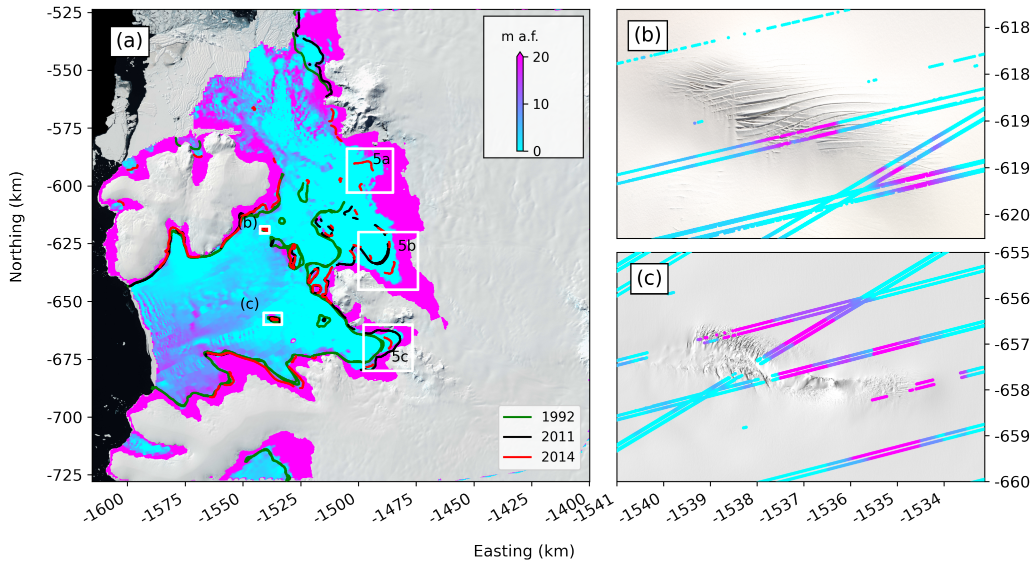

Figure 6. Height above flotation derived from ICESat-2 satellite laser altimetry and BedMachine ice thickness: (a) Rasterized using a 2D Gaussian kernel and locations of zoomed panels. Areas featuring a height above flotation > 200 m were masked out for visibility. The white rectangles show the location of panels in Figure 5 focusing on grounding-line retreat of tributary glaciers. (b) D2 in the Upper Dotson on top of a Planet SkySat Scene product acquired in December 2021, and (c) D5, also called the Wunneberger Rock nunatak, in the Lower Dotson over a DigitalGlobe Worldview-2 product from November 2021. Note the positive height above flotation of the ice upstream of these two pinning points, while the ice downstream quickly reaches a freely-floating state.

crevassing (Suppl. photos), while C5 ungrounded since 2015 during the retreat of Pope Glacier. Height above flotation shows the formation of a new C6 pinning point about 30 m a.f. with active surface crevassing (Suppl. photos).

Linearly extrapolated InSAR-derived retreat rates predict that the grounding line of Kohler Glacier will pass Kohler saddle within the next 4 years, effectively merging entirely into the catchment of Smith West Glacier within the next 15 years (Milillo et al., 2022). We therefore calculate the remaining height above flotation over Kohler saddle, which is about 170 m a.f. (Fig. 7b). Figure 7 also shows the newly formed pinning point C6, which currently features about $z_f = 30$ m a.f., as well as the D6 pinning point that ungrounded in 2014 (Scheuchl et al., 2016) and is characterized by $z_f = 0$ m a.f.

3.3 Surface-height change from satellite laser altimetry

We detect rapid surface-lowering rates spread across the Dotson-Crosson Ice Shelf System (Fig. 8a and b). From 2003 to 2016, surface lowering occurred mainly on the Crosson and its tributary glaciers with mean rates of 1.53±2.17 m/yr and up to 12.1 m/yr near the grounding line of Smith West Glacier. The Dotson thinned at a mean rate of 0.65± 1.06 m/yr with a local maximum of 6 m/yr near the grounding line of Kohler Glacier (Fig. 8a).

Surface-lowering rates largely increased between 2016 and 2020. The mean surface-lowering rate of the floating part of the Crosson increased by 19% to 1.82±2.55 m/yr,

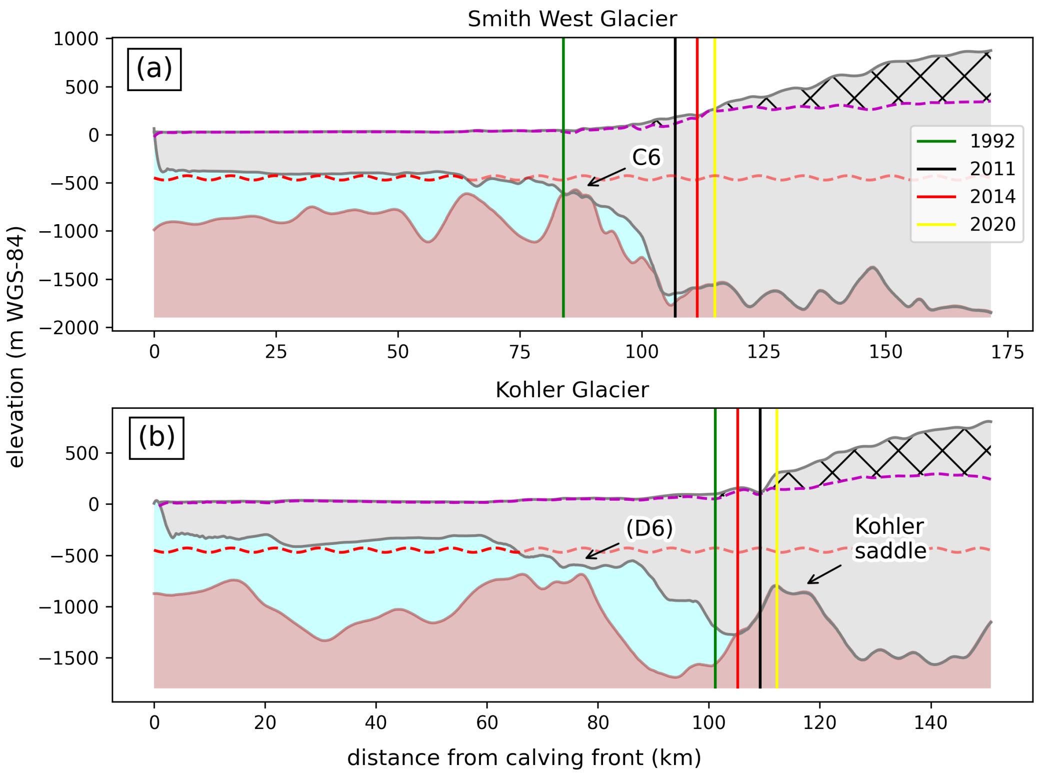

Figure 7. Profiles along flowlines of Smith West (Fig. 3a) and Kohler Glacier (Fig. 3b) from BedMachine with the dashed purple line indicating the level of flotation and the hatched areas the amount of ice that would raise global sea level if it were to melt. The dashed red wavy line indicates the schematic of the topmost level of mCDW (identified as conservative temperature $> 0°C$) from the CTD/LADCP profiles: (a) the newly emerged pinning point C6 on the Crosson, (b) the recently detached pinning point D6 in the Lower Dotson with the grounding-line retreat along a prograde slope nearing the bathymetric saddle underneath Kohler Glacier. Past grounding lines are from MEaSUREs (Rignot et al., 2017) and from (Milillo, 2021) in 2020. Note the readvance of Kohler Glacier between 2011 and 2014, which reversed between 2014 and 2020.

while its tributary glaciers, which reach over 100 km into the West Antarctic Ice Sheet, also experienced rapid surface lowering. Parts of Pope Glacier thinned at rates up to 16.6 m/yr, and Haynes Glacier further to the east up to 22.8 m/yr between 2016 and 2020. Large parts of the Smith Glaciers and Kohler Glacier thinned at rates of about 9 m/yr (Fig. 8b). The Dotson's surface lowered at an increased rate of 1.67±1.49 m/yr, particularly along a basal channel where surface-lowering rates were 2.36±1.65 m/yr. The combined surface lowering rate of Dotson and Crosson between 2016 and 2020 was 1.72±1.97 m/yr in mean and standard deviation. While regional surface lowering can be a result of both dynamic thinning and accelerated basal melting, the dynamic thickness change on floating parts of the Dotson is largely close to 0 m/yr (Fig. 8c), suggesting that basal melting is the dominant driver of ice-shelf thinning. This is counteracted by a surface mass balance of about 1±0.3 m/yr (Fig. 8d), which includes a negligible uncertainty when compared to its annual variability between 1979 to 2015.

We calculated the combined uncertainties in the rates of surface-elevation change between ICESat to REMA and REMA to ICESat-2 as the root sum of squared errors of the individual measurement techniques, divided by their time difference. ICESat data were acquired between 2003 to 2009 and have a vertical < 5 cm and horizontal < 15 cm accuracy (Brunt et al., 2019). The majority of the REMA tiles covering the Dotson-Crosson Ice Shelf area originate from 2016 and have an area-wide error of 5.5±0.9 m. ICESat-2 data, acquired between 2018 and 2020, provide absolute ice-surface elevations with $<$ 3 cm vertical and < 9 cm horizontal accuracies (Brunt et al., 2019). Altogether, these yield combined errors of 0.55 m/yr for the surface lowering estimate between ICESat (2006) and REMA (2016), and 1.83 m/yr between REMA and ICESat-2 (2019, Appendix B). We note the general agreement between the derived patterns of surface-lowering rates, which suggests that the true uncertainty is likely below the derived signals. Furthermore we expect the signals to be more reliable within the boundaries of individual REMA tiles, which were feathered along 100 km by 100 km tile boundaries to create a seamless mosaic (Howat et al., 2019).

With our height above flotation estimate derived earlier, it is possible to estimate when Kohler Glacier will merge into the catchment of Smith West Glacier if recent surface-lowering rates are extrapolated linearly into the future. Average height above flotation in this area is $z_f = 170$ m a.f. in 2020. Assuming that average surface lowering rates of 8.5 m/yr between 2016 to 2018/20 persist, our prediction for Kohler retreating past a saddle in the bed topography is 2040, which is slightly later than the prediction of 2035 from InSAR-derived grounding-line retreat rates (Milillo et al., 2022). This might be explained by the general landward bias of InSAR derived grounding lines when compared with our result from height above flotation and because both of these estimates are based on linear extrapolation with no physics involved.

3.4 Regional variability in basal melting

We now use mass-conservation principles to estimate the spatial distribution of basal melting from Lagrangian rates of surface lowering, dynamic thickness change and mean surface mass balance (Eq. 3). While basal melt rates are spatially variable, both ICESat and ICESat-2 observations agree that basal melting is most rapid close to the grounding line, where slopes at the ice base are steep and ice depth at the grounding zone is well in the realm of mCDW (Fig. 7). Basal refreezing is detected along Crosson's front in ICESat data (8 m/yr, Fig. 9a), and migrated about 6 km upstream in the ICESat-2 measurements, sporadically exceeding 10 m/yr, but over a much smaller area (Fig. 9b). Basal melting is generally weaker to the east, but pronounced to the west of the Dotson (about 25 m/yr); near the grounding line of Kohler Glacier (about 65 m/yr), where the seafloor is < -1600 m a.s.l. as well as in the upper reaches of the Crosson (91 m/yr). Qualitatively, this regional pattern of basal melting agrees well with results from the analysis of CryoSat-2 radar altimetry data between 2010 and 2016 (Gourmelen et al., 2017),

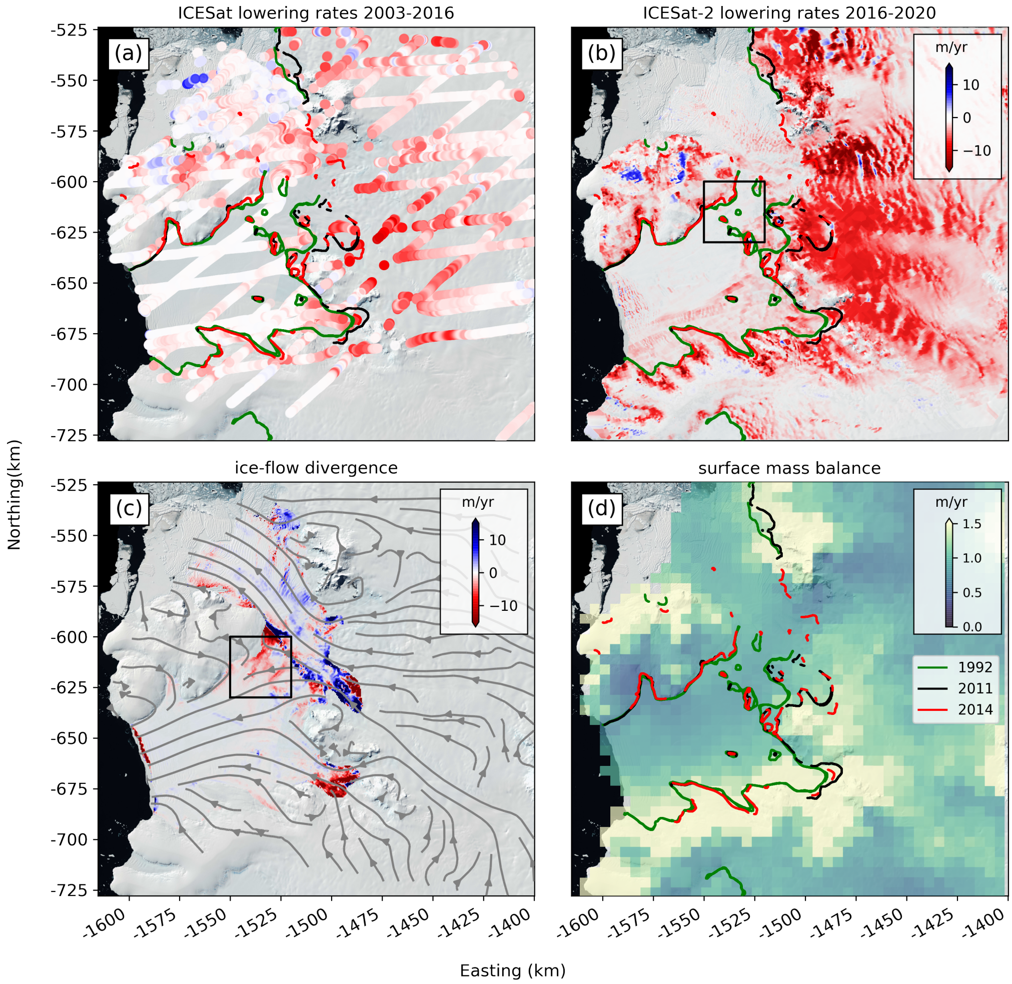

Figure 8. Components of the basal melt rate calculation from satellite laser altimetry: Lagrangian rates of surface lowering derived from differencing (a) ICESat and (b) ICESat-2 data with the Reference Elevation Model of Antarctica (REMA, Howat et al., 2019). (c) Dynamic thickness change and streamlines calculated from the MEaSUREs velocity field. Blue colors denote flow divergence, red colors flow convergence. Values are truncated to ±15 m/yr to maintain visibility and we also masked out surface-lowering signals within our uncertainty range of $\sigma z_s = 1.83$ m/yr. (d) Modeled mean annual surface mass balance in ice equivalent between 1979 and 2014 from RACMO2.3p1 (van den Broeke, 2019). Past grounding lines are from MEaSUREs (Rignot et al., 2017). The black rectangle in panels b and c show the spatial extent of Figure 11a and b in the Upper Dotson Ice-Shelf area, where field data were acquired in January 2020.

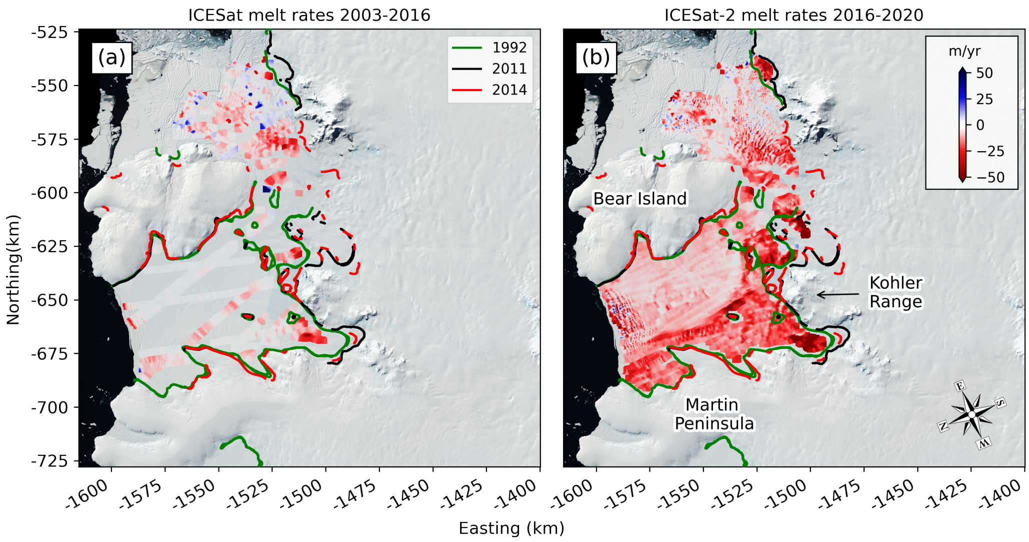

Figure 9. Rasterized Lagrangian basal melt rates from (a) ICESat and (b) ICESat-2 satellite altimetry data in combination with surface mass balance modeling and ice dynamics. Red and blue colors indicate basal melting and refreezing, respectively. The applied mass conservation technique relies on hydrostatic equilibrium in both the freeboard to ice thickness inversion and the assumption of negligible vertical shear stress within the ice. We therefore masked out non freely-floating areas delineated by tidal flexure modeling. We also masked out signals within our uncertainty range of $\sigma\dot{m}_{\mathrm{b}} = 2.1$ m/yr.

and their regional average of 6.1±0.7 m/yr for the Dotson is within the 4.88±6.99 m/yr range between 2003 and 2016 derived in this study. Extending the ICESat record with more recent ICESat-2 data suggests a trifold acceleration in basal melt to 15.86±10.75 m/yr from 2016 to 2020. The higher spatial coverage of ICESat-2 also allows us to capture basal-melt rates along a narrow channel that reaches from the Upper Dotson, past the D4 and D5 pinning points, to the ice-shelf front. Our results confirm previous work by Gourmelen et al. (2017) that this channel is actively evolving along its entire length but with accelerated basal-melt rates around 22 m/yr. Particularly high melt rates within this channel are identified at the confluence of two basal channels in the Upper Dotson near D4 (50 m/yr), to the east of D5 (55 m/yr) and near its origin in the Upper Dotson (45 m/yr). Our calculations also indicate that mean basal-melt rates doubled underneath the Crosson from 5.51 ± 10.24 m/yr to 11.48 ± 13.65 m/yr over the same time period.

Using error propagation techniques, we combine uncertainties in the rates of surface elevation change with errors in mean ice-column density, ice-velocity fields and surface mass balance and estimate a combined uncertainty in basal melt rates of $\sigma\dot{m}_{\mathrm{b}} = 0.8$ m/yr for 10 years between ICESat to REMA and $\sigma\dot{m}_{\mathrm{b}} = 2.1$ m/yr for 3 years between REMA to ICESat-2 (Appendix B). While these large uncertainties originate mainly from errors in REMA, they are still about one order of magnitude smaller than our derived signals of mean basal melt.

4 Discussion

4.1 Intrusion and pathways of modified Circumpolar Deep Water

We now compare the derived regional patterns in basal melting with new oceanographic measurements of ocean current and temperature acquired along the front of Dotson between January 21 and February 7, 2022 (Fig. 10). The CTD/LADCP profiles are vertically-averaged between the seabed and ice draft, and show that mCDW enters the sub-ice-shelf cavity as a strong and narrow jet approximately 5-km wide at the eastern side of the ice shelf (Fig. 10), with maximum conservative temperature of 0.5-0.6°C below 600 m depth (not shown). The inflow is deep enough to not interact with the base of the ice shelf in the eastern side of Dotson. The inflowing mCDW interacts with the base of the ice shelf likely near the grounding line, which helps to explain the larger basal melt rates observed in those locations (Fig. 9). Glacially-modified mCDW leaves the cavity as a strong and narrow jet ($\sim$ 2 km) at the western side of the ice shelf (Fig. 10) at 200-500 m depth with conservative temperatures between -1 and 0°C (not shown). Our measurements support the existence of a clockwise ocean circulation underneath the Dotson, in agreement with previous studies (e.g., Randall-Goodwin et al., 2015; Yang et al., 2022), suggesting that it is a persistent feature, at least since the first measurement. The mCDW that interacts with the freshwater from the basal melting gains buoyancy and ascends near the base of the ice (although it conserves substantial heat), which supports a shallower ocean circulation pattern. This clockwise and shallow circulation coincides with areas of pronounced basal melting in the Lower Dotson (Fig. 9), where mCDW freshens and forms a buoyant meltwater plume near the ice-shelf base, exiting the cavity near Martin Peninsula (Fig. 10). The circulation pattern is consistent with results from Dutrieux et al. (2018) who deployed three Seagliders and four EM-APEX floats to sample oceanic properties beneath the Dotson and identified deep inflowing warmer water on the eastern side of the sub-ice-shelf cavity and shallower outflowing meltwater on its western side.

The changes observed at the grounding line (Fig. 9) could be associated with large-scale variations on the supply of mCDW onto the continental shelf. The amount of mCDW supplied to the continental shelf in the Amundsen Sea is driven by the strength of the eastward wind at the shelf break (e.g., Wåhlin et al., 2013; Kim et al., 2017; Dotto et al., 2020). The intensity of the eastward wind-stress anomaly at the shelf break has increased in the last 100 years due to the southward migration of the westerly wind belt, at least for the eastern Amundsen Sea (Holland et al., 2019). Due to short temporal extent of hydrographic measurements in the Dotson-Getz trough, it is not clear if the availability of mCDW has increased in recent years in the area. Evidence for a decadal variability impacting the heat content of the ocean in front of Dotson was shown by Jenkins et al. (2018); they showed periods of high temperatures and high meltwater flux in the late-2000s and early-2010s, whereas low temperatures and low melting were observed in the early-2000s and mid-2010s. The rate of grounding-line retreat in the Amundsen Sea is currently influenced more by those successive strong decadal warm periods, triggering episodic retreats, rather are more likely to trigger episodic retreats of the grounding line than a progressive ocean warming in the region (Jenkins et al., 2018). Recent observations suggest a relatively fast time-scale ($\sim$2-month lag) between the variability of heat transport inflowing the Dotson cavity and the meltwater outflowing at the western Dotson (Yang et al., 2022). Ocean-driven basal melting can change the sub-ice-shelf cavity geometry, increasing water-column thickness, which in turn enhances the volume of circulated ocean water beneath the ice shelf. Past works have suggested that a stronger circulation and exposed ridges could alter turbulence and mixing under the ice shelf, which might increase the ice melting through higher heat fluxes at the ice-ocean interface (e.g., Jacobs et al., 2011). In any case, an increase in the inflow of mCDW and modification at the grounding line can intensify the outflow of the buoyant meltwater on the western Dotson, with potential impacts on the erosion of the Lower Dotson and a collapse of the ice shelf (e.g., Gourmelen et al., 2017). Given the vertical extension of mCDW

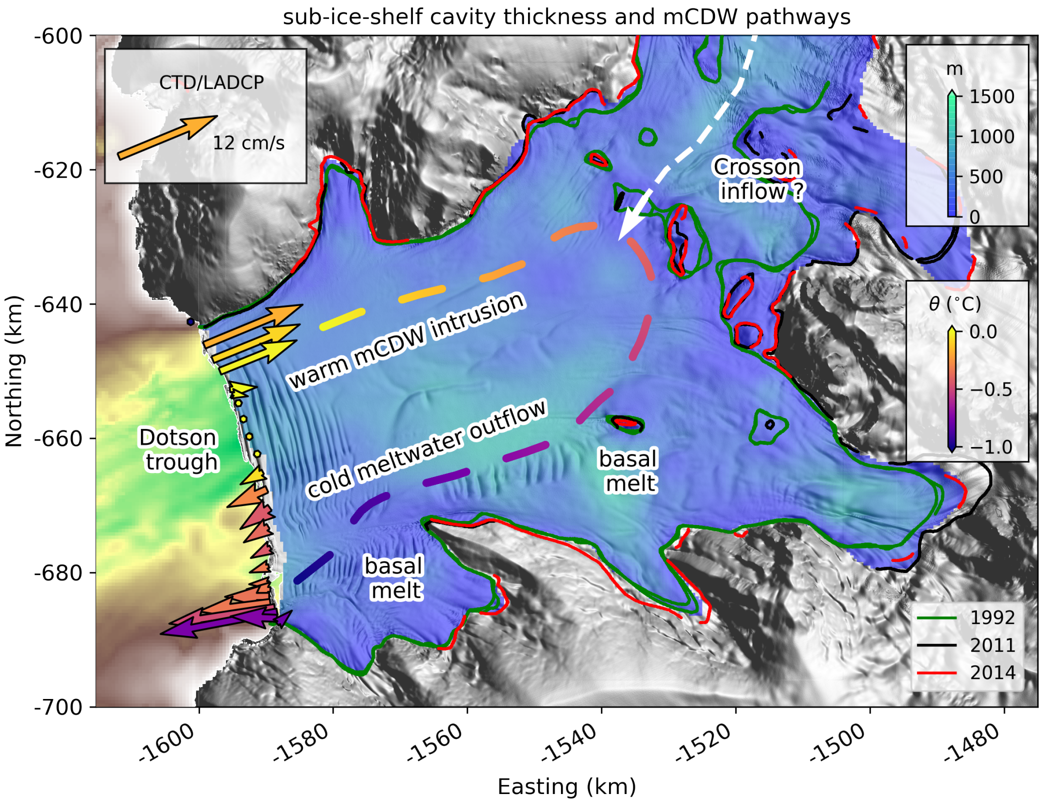

Figure 10. De-tided ocean flow below the ice draft along the Dotson's front derived from ship-based CTD/LADCP profiles in early 2022. The color of the arrows indicates vertically-averaged conservative temperature below the ice draft. Note water inflow to the east and outflow to the west. The dashed line is a schematic of the possible mCDW pathway beneath the ice shelf.

at eastern Dotson (upper inflow at ∼450 m; Fig. 7), Kohler saddle will be flooded with mCDW with continued retreat of the grounding line. This will lead to new pathways where mCDW can access the ice-shelf grounding zone with the potential to increase the rate of grounding-line retreat as a new deep cavity opens up.

4.2 Spatial and temporal patterns of basal melt

Gourmelen et al. (2017) used CryoSat-2 interferometric-swath radar processing to measure a mean surface lowering rate of 0.26±0.03 m/yr for the Dotson between 2010 and 2016. Their rate is consistent with 0.28±0.03 m/yr between 1994 and 2012 derived from the satellite radar altimeter record (Paolo et al., 2015). Our surface-lowering rates derived from the combination of ICESat altimetry data with REMA are 0.65±1.06 m/yr between 2003 to 2016 and entail a relatively large uncertainty of 0.55 m/yr compared to previous research. We note, however, broad agreement in the regional patterns of thinning and grounding-line retreat between the different methods. Our results, in turn, suggest a recent increase in basal melt rates from 2003/16 to 2016/20 that corresponds to a net meltwater increase at the ice-shelf base from 26.9 to 87.3 Gt/yr on Dotson (5505 km^2) and from 18.8 to 39.2 Gt/yr underneath Crosson (3411 km^2), respectively. Randall-Goodwin et al. (2015) used hydrographic data acquired in 2011 to estimate 81 Gt/yr of meltwater, which further supports our finding that the ocean forcing increased and is directly translated to the observed higher basal-melt rates underneath the floating ice shelves. The increase of basal melting is particularly high underneath the Lower Dotson (Fig. 9), where the ice-flow speed slowed down over the same time period (Fig. 3b).

4.3 Changes of ice-shelf pinning points

The Upper Dotson features several ice-shelf pinning points between Bear Island and the Antarctic continent, indicating that bathymetry in this area is very variable (Fig. 1c) and water-column thickness consequently shallow. Modeling experiments by Mueller et al. (2012) show that a shallow sub-ice-shelf cavity locally enhances tidal currents and thus the heat exchange at the ice-ocean interface through turbulent heat transfer. This mechanism may result in locally increased basal melt particularly in the vicinity of pinning points where bathymetric highs have the potential to streamline tidal currents into the sub-ice-shelf cavity. Pinning points stabilize ice shelves through shear stresses at the ice-base (Matsuoka et al., 2015). Their ungrounding is known to precede ice-shelf disaggregation and rapid grounding-line retreat (Goldberg et al., 2009; Favier et al., 2012; Favier & Pattyn, 2015; Favier et al., 2016; Reese et al., 2018; Wild et al., 2022).

We therefore investigate a local thickening signal upstream of D2 with rates up to 7.5 m/yr (Fig. 11a). This is of particular interest because upstream thickening indicates significant resistance to the ice flow, such as observed near D5 in the Lower Dotson (Fig. 6c), which in turn is important for net ice-shelf buttressing. Thickening at D2 may be a result of (i) relative compression preceding the redirection of ice flow, (ii) advection of a thicker ice bulge from the ungrounded D1 pinning point since the late 1990s, or (iii) mismatches in the calculation of Lagragian elevation change because of inaccuracies in either the velocity record or REMA. To rule out (i) we calculate the dynamic thickness change and find pronounced convergence only a few km further upstream of D2 with rates up to 6 m/yr (Fig. 11b), while the ice-flow closer to the pinning point converges only at about 1.8 m/yr, which only partly explains the observed thickening rate. To estimate (ii) we compile all available Landsat panchromatic imagery between 1973 and 2020 and monitor the ice-advection process in the Upper Dotson throughout the 2000s until the end of the record in 2020 (Suppl. video). Thickening between 2016 and 2020 because of advection of the ice-bulge onto D2 can therefore not be ruled out using the Landsat record alone.

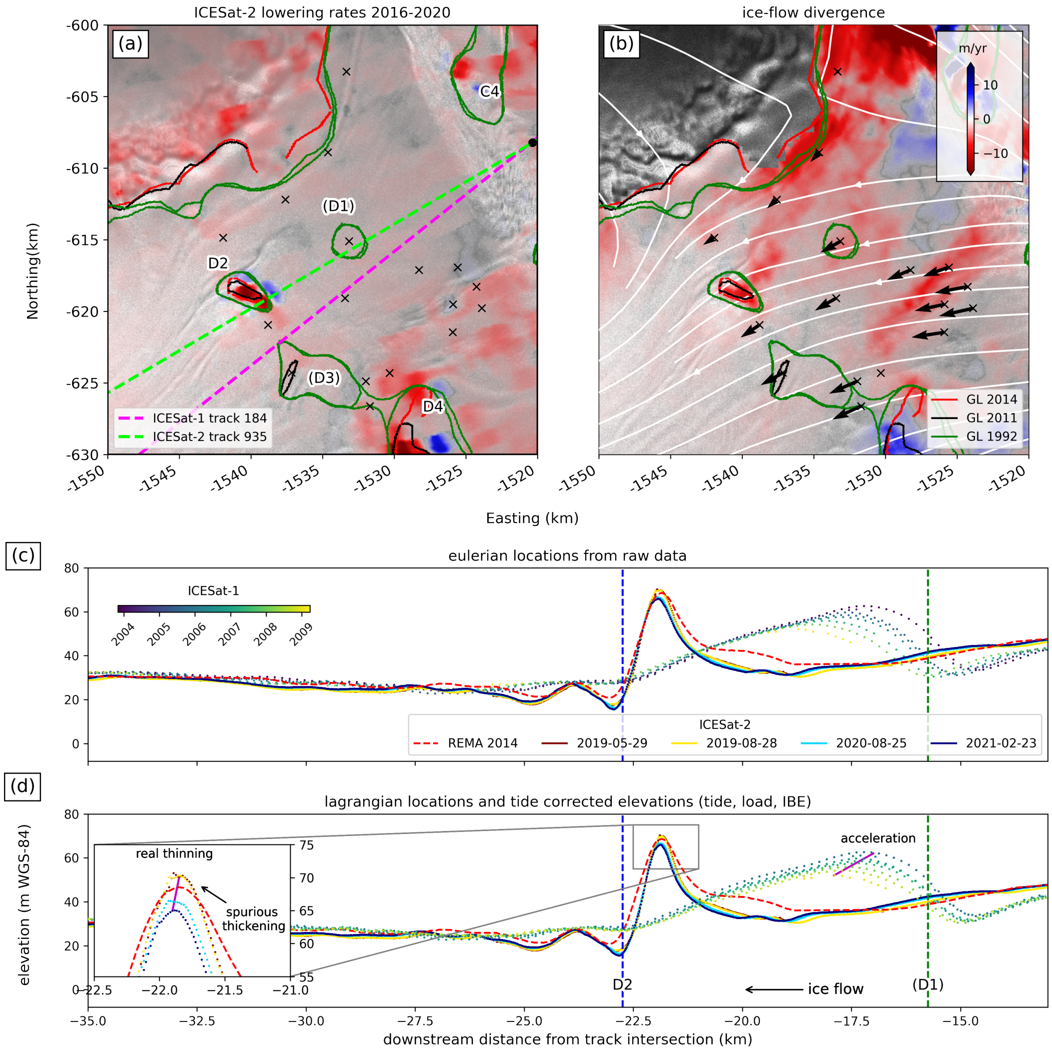

Figure 11. Investigation of a thickening signal upstream of the D2 pinning point: (a) Lagrangian surface lowering rates derived from ICESat-2 data and the REMA surface elevation model showing a spurious thickening signal upstream of D2. The two dashed lines show the location of the ICESat and ICESat-2 altimetry tracks in panels (c) and (d). The black crosses show field sites where in-situ data were acquired in Jan. 2020. (b) Dynamic thickness change, streamlines and arrows of GPS-derived surface velocity used for validation. (c) Progressive ungrounding of D1 and advection of a thicker ice bulge towards D2 throughout the 2000s. Note the relative acceleration of the ice flow in the ICESat data indicated by the magenta line in the main panel d and Eulerian locations of more recent ICESat-2 data along a nearby track that crosses the D2 pinning point. (d) Migrated and tide-corrected ICESat-2 data from 2019 and the REMA data cause a spurious thickening signal upstream of D2, while local ICESat-2 peaks in the zoomed inset clearly show a surface lowering signal of about 2.8 m/yr (indicated by the purple line in the inset).

To further investigate the ice advection process, we monitor altimetry data along two individual ICESat and ICESat-2 tracks in the Upper Dotson (Fig. 11a). The Eulerian locations show that the remaining ice-bulge from D1 traveled about 1.7 km between the first delineation of its grounding line in 1992 and early 2004 when the first ICESat measurements were acquired (Fig. 11c), effectively dating the ungrounding of D1 to the late 1990s given an average ice-flow speed of 220 m/yr. We migrate all subsequent ICESat data to 2004 as well as correct for ocean tides and atmospheric variability and find that the remainder of D1 lost about 10 m of ice-shelf surface elevation between 2004 and 2009 (or 2 m/yr). Lagrangian locations of D1's advecting ice-bulge are not perfectly aligned vertically, indicating that ice-flow speed increased by up to 150 m/yr over the 6 years beyond what is captured in the velocity record used for the migration (purple line in Fig. 11d).

We also migrate all ICESat-2 data to the nominal date of REMA and find that REMA underestimates the height of D2 in 2014 when compared to the later ICESat-2 measurements. This indicates either thickening of D2 between 2014 and the first acquisition of ICESat-2 data in 2019, or is a consequence of inaccuracies in REMA ($\delta z_s = 5.5$ m). In either case, differencing REMA and ICESat-2 data from 2019 introduces a spurious thickening signal just upstream of D2 that is not evident when comparing individual ICESat-2 data alone, which yields an increased surface lowering rate from 2 m/yr to about 2.8 m/yr. Although temporary thickening between 2014 and 2019 is possible given that the ice-bulge advection since the late 1990s is still ongoing, ICESat-2 data clearly show evidence of surface lowering since 2019. With a current height above flotation of up to 26 m, D2 will unpin from its bathymetric high point in less than 10 years if contemporary surface lowering rates remain constant.

The Lower Dotson, in turn, shows clear proof of pinning-point destabilization with D6 ungrounding entirely in the early 2010s (Figs. 5a and 6b, Scheuchl et al., 2016). With ice-flow slowing down considerably over the same time (Fig. 3b and d), a thickening of the ice-column and thus increased grounding of D6 would have been expected. In the absence of surface ablation (Fig. 8d), the ungrounding of D6 during the simultaneous deceleration of the Lower Dotson is therefore directly tied to an unproportional thinning of the ice shelf and an indicator for the ongoing destabilization of the Lower Dotson.

4.4 Interpretation of observed dynamic response

With the increased availability of mCDW in the Amundsen Sea and its access into the sub-ice-shelf cavity underneath Dotson and Crosson, basal-melt rates accelerated particularly in the Lower Dotson and around ice-shelf pinning points, whose ungrounding reflect the bathymetry-driven pathways of mCDW intrusion. However, ice flow of the Lower Dotson decelerated, although all other indicators of structural integrity, tri-fold increase in ocean forcing and ungrounding of the D6 pinning point in 2014, point towards significant destabilization. We hypothesize that slow-down of the Lower Dotson is attributed to the interplay of acceleration in the Upper Dotson, following the reported ungrounding of the D1 and D3 ice-shelf pinning points, and subsequent plugging of inflow from the Kohler Glacier. Conversely, grounded parts of Smith West Glacier disproportionately accelerated in tandem with the retreat of Crosson, effectively re-routing ice discharge from the Kohler Glacier into the catchment of Smith West Glacier. We attribute flow acceleration of both Smith West and East Glaciers not only to the weakening of the Crosson's margins and overall diminishing ice-shelf buttressing, but it may also be a clear example of marine ice-sheet instability already at play at its tributary glaciers.

Ungrounding of the C1, C2, C3, and C5 pinning points in the mid 2010s preceded the disaggregation of Crosson. The loss of sufficient ice-shelf buttressing, and the associated rapid grounding-line retreat, have led to a drastic speed-up in ice flow, which is still evolving (Fig. 3). The acceleration of Smith West Glacier then drew ice discharge

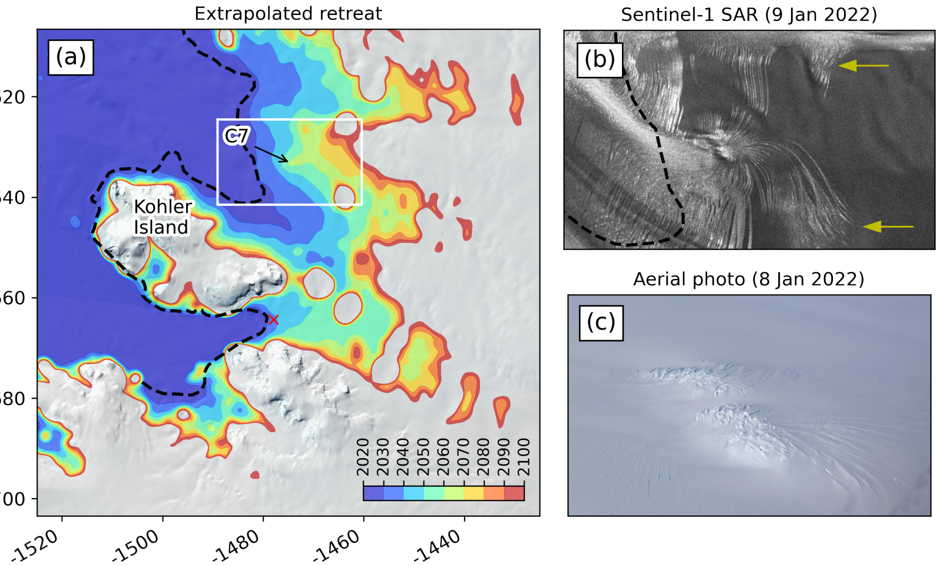

Figure 12. (a) Extrapolated grounding-line evolution from height above flotation of the Dotson-Crosson Ice Shelf System, assuming surface lowering rates between 2016 and 2020 to remain steady throughout the 21st century. Note that the grounding line will retreat across Kohler saddle (red cross) between 2030/40, and effectively merge Kohler Glacier entirely into the Smith West catchment by 2050/60. (b) Sentinel-1 Synthetic Aperture Radar image acquired on 9 Jan 2022 showing the new C7 pinning point and localized areas of surface thickening indicated by yellow arrows. (c) Timely aerial photograph of active surface crevassing on C7, photo courtesy of Jesse Norquay. The black dashed line delineates the most recent grounding line from (Milillo, 2021).

from Kohler Glacier, effectively starving ice inflow into the Lower Dotson. In the absence of any upstream bathymetric ridges to inhibit marine ice-sheet instability (Fig. 1c), it is crucial to assess the integrity of Crosson's last remaining pinning points C4 and C6 (Fig. 7a) to determine future retreat patterns in the region, which will likely trigger further destabilization of the Lower Dotson via the complex interplay between Kohler and Smith West Glacier. Both pinning points lie along a significant shear zone (Fig. S1c), where rheologically weaker ice will continue to progressively decouple the Upper Dotson from Crosson. Further downstream near the ice-shelf edge, calving events between 1973 and 1988 have been recorded in the past to reduce the ice front by 5 to 7 km on Dotson and 10 km on Crosson (Lucchitta et al., 1994), but have not been observed since. Continued disaggregation of Crosson supports our observations that C4 and C6 are losing their structural integrity.

4.5 Future change in the Dotson-Crosson Ice-Shelf System

Combining our derived maps of height above flotation and surface-lowering rates of grounded ice allows us to linearly extrapolate the regional destabilization of tributaries of the Dotson-Crosson Ice Shelf system into the future. We divide height above flotation by surface lowering rates and smooth the noise using a 2D Gaussian kernel to derive grounding-line contours until the end of the 21st century (Fig. 12a).

The extrapolation indicates that with the grounding line of Kohler Glacier merging into the catchment of Smith West Glacier, the Kohler Range will be cut-off from Antarctica's main land by the end of the 21st century to form a large island between the remainders of Dotson and Crosson, which we call Kohler Island. The grounding lines of Pope, Smith East/West Glaciers and Kohler Glacier would continue to retreat along their respective bathymetric/topographic troughs. Extrapolated retreat for Smith West Glacier is over 50 km in 80 years, corresponding to a mean grounding-line-retreat rate of 0.6 km/yr. This is 3 to 4 times slower than its recent maximum retreat rates of 2 km/yr observed between 2016 and 2018 (Milillo et al., 2022), suggesting that either our estimates are at the lower end of the possible range or that the recently observed high retreat rates were only short-lived.

Most contemporary ice-shelf pinning points will disappear in the next 1 to 3 decades with only the D5 nunatak, i.e. Wunneberger Rock, buttressing the Lower Dotson into the 22nd century. In the Upper Dotson, D2 will likely unground within the next decade and is outlived by the relatively well-grounded D4 pinning point which will likely remain into the second half of the 21st century. On the Crosson, C6 is likely ungrounded by 2050 and is followed by the newly formed C7 pinning point around the year 2070 (inset in Fig. 12a). The C7 pinning point is currently at the center of an active crevasse zone that is evident in satellite radar imagery (Fig. 12b) and aerial photography (Fig. 12c). The extrapolation also indicates that a few other pinning points may emerge during deglaciation, such as near the Smith East/West Glaciers and near Kohler Glacier (Fig. 12a). With the absence of any bed-topographic highs in those regions (Fig. 1c), we interpret these as artifacts of extrapolating localized surface thickening rates (Fig. 8b), where the ice-flow converges such as against Kohler Island (Fig. 1b), and not the real formation of new pinning points. In any case, the formation of these relatively small pinning points such as C7 clearly does not provide the necessary buttressing for regional restabilization once rapid ice-flow acceleration takes place. Counter-intuitively, recent research around Thwaites Glacier suggests pinning points can also be a destabilizing feature in advanced stages of ungrounding, because of the possibility of backstress-triggered failure from accumulated damage (Benn et al., 2021).

Removal of ice-shelf buttressing is of particular concern because it typically triggers significant grounding-line retreat and acceleration of tributary glaciers (Scambos et al., 2004; Rack & Rott, 2004). Rapid grounding-line retreat after ice-shelf disaggregation could theoretically be mitigated by retreat into a fjord-like valley, because of the increase in lateral stresses between narrowing side walls (Gudmundsson, 2013). However, the width of the subglacial valley underneath Smith and Kohler Glaciers remains constant over more than the next 50 km (Rignot et al., 2014, Fig. 1c) with a retrograde submarine bed that is rendering them dynamically unstable (Weertman, 1974; Schoof, 2007). With an inland-thickening ice column, the amount of ice above its flotation level is continuously increasing upstream (Fig. 7) and thus the potential sea-level contribution is steadily increasing. In the absence of significant bathymetric ridges and well-grounded pinning points, it can be expected that discharge rates of the Smith West Glacier are continuing to increase (Fig. 7a). Whether the onset of marine ice-sheet instability across Kohler saddle would reverse ice flow into the Lower Dotson and potentially delay regional destabilization of the Dotson-Crosson Ice-Shelf System remains to be investigated. The complex interplay of this process, however, is strongly controlled by the basal topography near Kohler saddle and the dynamic linkages between the glaciers feeding the Dotson and Crosson.

5 Conclusion

Both the Dotson and Crosson are destabilizing, despite apparent signals of restabilization such as a decrease in ice-flow velocity (Fig. 3b) and the appearance of a new pinning point (Fig. 12). Deceleration of the Lower Dotson is due to an interplay of reduced ice inflow from the feeder Kohler Glacier (Fig. 4) and past acceleration of the Upper Dotson that temporarily buttressed inflow to the Lower Dotson (Fig. 3a). Our results from integrating ICESat and ICESat-2 laser altimetry data with available field data confirm that the grounding lines of Pope, Smith West/East and Kohler Glaciers continued to retreat (Fig. 5) and that a number of stabilizing ice-shelf pinning points ungrounded (Figs. 6 and 7). We link both the retreat and the ungrounding events to a recent acceleration of basal melt underneath the thicker areas of floating ice (Fig. 9). Ship-based measurements in front of the Dotson show warm mCDW pathways into the sub-ice-shelf cavity (Fig. 10). With Kohler Glacier's grounding line currently retreating past a bathymetric saddle (Fig. 7), and effectively merging into the catchment of Smith West Glacier by the middle of the 21st century (Fig. 12), it can be expected that mass input into the Lower Dotson will be considerably reduced. Whether the Dotson will thin and/or disaggregate in the aftermath of this transition, similar to how the Crosson has evolved, remains to be investigated, because a small number of well-grounded pinning points will continue to stabilize the Dotson into the next century.

Continued ocean-forced thinning of the Crosson will likely result in retreat of its ice front far upstream of the current extent. This will greatly reduce ice-shelf buttressing on the tributary Pope and Smith Glaciers, and will likely cause further grounding-line retreat and destabilization of this part of the West Antarctic Ice Sheet. The asymmetric retreat of the grounding line will soon open up new pathways for mCDW intrusion. Continued research on this area will provide important paths to investigate the processes that drive regional destabilization of ice masses in the Amundsen Sea sector, but on a much smaller, more tractable, scale (kilometers) and over a shorter time-frame (decades) than the retreat of Thwaites Glacier (centuries to millennia).

Here, we identify a few natural laboratories on the Dotson-Crosson Ice-Shelf System for future research: (i) the deep bathymetry downstream of Kohler Glacier's grounding line (Fig. 1c), where the intrusion of warm mCDW concurs with an area of pronounced ice-thickness convergence (Fig. 8c) to cause high basal-melt rates underneath the Lower Dotson (Fig. 9b); (ii) the confluence of two basal channels in the Upper Dotson, where glacially modified mCDW may enter the sub-ice-shelf cavity from the Crosson to further accelerate basal melting around the last remaining ice-shelf pinning points (Fig. 9b); (iii) Kohler saddle, where the exact shape of the bedrock underneath the grounded ice (Figs. 7b and 12a) will determine the retreat rates into the catchment of Smith West Glacier that is anticipated for the late 2030s; (iv) the D2 pinning point, which is likely to unground within the next decade (Fig. 11); and (v) the newly discovered D7 pinning point near the grounding line of Smith East Glacier (Fig. 12). All these sites could be studied with coupled atmosphere-ocean moorings that capture in tandem the effects of the different systems on the ice shelf evolution, such as deploying Automated Meteorology-Ice-Geophysics Observing Stations (Scambos et al., in prep.).

6 Open Research

We used the NASA Making Earth System Data Records for Use in Research Environments (MEaSUREs) Program, Version 1 and 2, Antarctic-wide ice surface velocity products (Rignot et al., 2014, 2017) and the Inter-mission Time Series of Land Ice Velocity and Elevation (ITS_LIVE) product (Gardner et al., 2019). For ice thickness and bathymetry/bed topography the products from BedMachine version 2 (Morlighem, 2020). Surface elevations are from the Reference Elevation Model of Antarctic (REMA) digital elevation model (Howat et al., 2019), the ICESat Level-2 GLAH12 release 634 global altimetry data (Zwally et al., 2014) and the ICESat-2 ATL06 land ice data release, Version 3 (Smith et al., 2019). We used the EIGEN6c4 geoid model (Förste et al., 2014) for mean sea level, the Regional Atmospheric Climate MOdel (RACMO) version 2.3 (Lenaerts et al., 2018) and the logarithmic strain rate software (Alley et al., 2018). Past grounding lines are from Rignot et al. (2017) and Milillo (2021). Ocean tides and tidal loading from the Circum-Antarctic Tidal Solution (CATS2008) model (Padman et al., 2002, 2008) and the fully global barotropic assimilation (TPXO9) model (Egbert & Erofeeva, 2002). Surface weather observations provided by the University of Wisconsin-Madison Antarctic Meteorology Program. The COMSOL Multiphysics finite-element software for modelling of tidal ice-shelf flexure. The GAMIT/GLOBK GPS processing software version 10.71 (Chen, 1998). The LDEO-IX toolbox (Thurnherr, 2018) and the TEOS-10 toolbox (McDougall & Barker, 2011) for processing of LADCP data. Map background is the Landsat Image Mosaic of Antarctica (Bindschadler et al., 2008).

Output products shown in our figures (such as the α map, height above flotation, surface lowering, dynamic ice thickness change, basal melting and grounding-line extrapolation maps as well as ship-based measurements of ocean current) are available through the US Antarctic Program Data Center (`https://doi.org/10.15784/601578`). We would appreciate citation of our paper if you think these data are useful for your own research.

Appendix A Uncertainty of Lagrangian migration

We estimate ice-flow speed errors from GPS measurements in the Upper Dotson to -0.9 ± 13 m/yr, with a directional error of 4 ± 6 degree in mean and standard deviation (Fig. 2a and b). These uncertainties, however, add up over several years for consecutive migration of altimetry points. We therefore pick 10000 randomly sampled altimetry points and migrate them within both the speed and directional ranges for 10 and 3 years, corresponding to the mean time difference between ICESat to REMA and REMA to ICESat-2 data acquisition. After the migration, we find all points within 3 standard deviations to fit an uncertainty ellipse that shows a 98.9% confidence level. The enclosed area sums up to 537 m^2 and 193 m^2 for 10 and 3 years respectively (Fig. A1). Given a grid resolution of 40 m by 40 m, individual points may migrate up to 2 grid cells and 1 grid cell outside our estimate in Easting, but remain within the same grid cell in Northing direction.

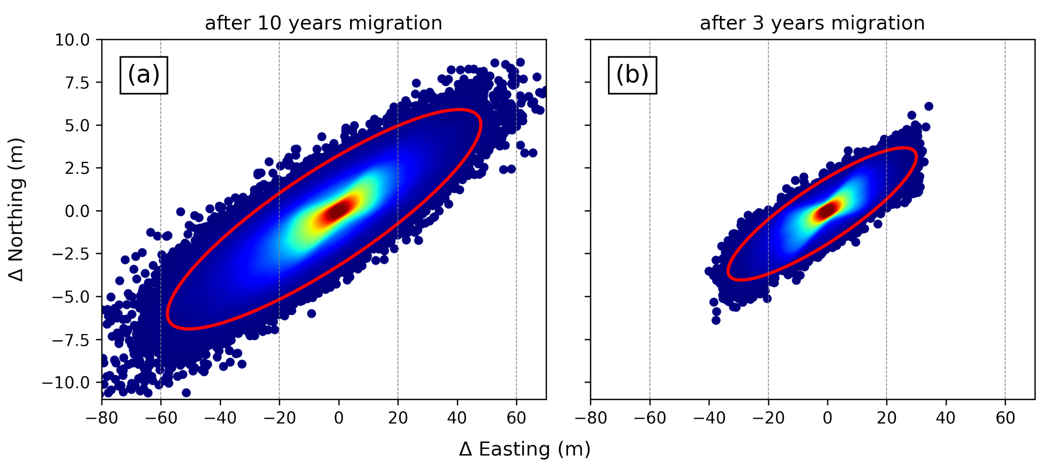

Figure A1. Anomalies of migrated point coordinates given the errors in the velocity field: (a) after 10 years such as between ICESat and REMA, and (b) after 3 years such as between REMA and ICESat-2. The red confidence ellipses enclose 98.9% of the points and were derived using the Pearson correlation coefficient. Colors indicate point density and confirm a normal distribution of points. The vertical dashed gray lines show our grid resolution of 40 m by 40 m.

Appendix B Uncertainty of basal melt rates

To estimate uncertainty of basal melt rates, we propagate the individual errors through Eq. 3 from the main text (rearranged here for simplicity):

$$\mathbf{\dot{m}_b} = \frac{\mathrm{D}\mathbf{H}}{\mathrm{D}t} + \mathbf{H}(\dot{\epsilon}_{\mathbf{lon}} + \dot{\epsilon}_{\mathbf{trans}}) - \mathbf{\dot{m}_s} \tag{B1}$$

The combined uncertainty, $\sigma\dot{\mathrm{m}}_{\mathrm{b}}$, can then be expressed as:

$$\sigma\dot{\mathrm{m}}_{\mathrm{b}} = \sqrt{\sigma_1^2 + \sigma_2^2 + \sigma_3^2}, \tag{B2}$$

with the three terms on the right hand side as follows:

$$\sigma_1 = \frac{\sqrt{\sigma^2_{\mathrm{H_{REMA}}} + \sigma^2_{\mathrm{H_{IS/2}}}}}{\mathrm{D}t}, \tag{B3}$$

$$\sigma_2 = \mathrm{H}\sqrt{\sigma^2_{\dot{\epsilon}_{lon}} + \sigma^2_{\dot{\epsilon}_{trans}}}, \tag{B4}$$

$$\sigma_3 = \sigma_{\dot{\mathrm{m}}_{\mathrm{s}}} \tag{B5}$$

To find the uncertainty for the first term (Eq. B3), we calculate sensitivity coefficients using a perturbation method that allows us to combine errors with different units of measure (ice surface elevation in m a.s.l. and mean ice column density of $\rho = 890 \pm 5$ kg/m3):

$$\sigma\mathrm{H_{IS/REMA/IS2}} = \sqrt{(c_1\delta\mathrm{z_s})^2 + (c_2\delta\rho)^2} \tag{B6}$$

With the sensitivity coefficients $c_1 = \frac{\delta\mathrm{H_{z_s}}}{\delta\mathrm{zs}}$ and $c_2 = \frac{\delta\mathrm{H}_\rho}{\delta\rho}$. Given the vertical $<$ 5 cm and horizontal $<$ 15 cm error of ICESat surface elevations, these perturbations are $\delta\mathrm{z_s} = \sqrt{(0.05\mathrm{m})^2 + (0.15\mathrm{m})^2} < 0.16$ m, and $\delta\mathrm{z_s} = 5.5$ m for REMA. The $<$ 3 cm vertical and $<$ 9 cm inaccuracy of ICESat-2 results in $\delta\mathrm{z_s} < 0.09$ m. Determining the sensitivity coefficients requires the use of a mean surface elevation from ICESat, REMA and ICESat-2 data over the freely-floating ice shelf. These are 34.2, 33, 24.8 m a.s.l, respectively, and yield mean ice thicknesses of 256.2, 247.4 and 185.6 m (note these are absolute values for perturbation purposes and not relative to the geoid as our freeboard calculations). We can now calculate the effect of each perturbation on the mean ice thickness as follows:

$$\delta\mathrm{H_{z_s}} = (\mathrm{z_s} + \delta\mathrm{z_s})\frac{\rho_{sw}}{\rho_{sw} - \rho} - \mathrm{H}, \tag{B7}$$

$$\delta\mathrm{H}_\rho = \mathrm{z_s}\frac{\rho_{sw}}{\rho_{sw} - (\rho + \delta\rho)} - \mathrm{H}, \tag{B8}$$

which are inserted in B6 and results in $\sigma\mathrm{H_{IS/REMA/IS2}} = 3.6$ m for ICESat and 4.2 m for both REMA and ICESat-2 data. According to B3 $\sigma_1 = 0.6$ m/yr over the 10 years between mean ICESat data acquisition (2006) and the mean time-stamp of the REMA mosaic (2016), and $\sigma_1 = 2.0$ m/yr over the 3 years to the mean acquisition date of ICESat-2 data (2019).

To determine the uncertainty of the second term B4, we multiply the three mean ice thicknesses stated above with the uncorrelated errors in the longitudinal and transverse strain rates of $4 * 10^{-4}$ m/yr, which results in $\sigma_2 = 0.14$, 0.14 and 0.1 m/yr for ICESat, REMA and ICESat-2, respectively.

The uncertainty of the third term B5 is calculated from the standard deviation of the annual mean surface mass balance between 1979 to 2015, which is treated as a constant and therefore $\sigma_3 = 0.3$ m/yr. Altogether, the combined uncertainty in basal melt rates B2 yields $\sigma \dot{\mathrm{m}}_{\mathrm{b}} = 0.8$ m/yr for ICESat to REMA and $\sigma \dot{\mathrm{m}}_{\mathrm{b}} = 2.1$ m/yr for REMA to ICESat-2.

Appendix C Uncertainty of height above flotation

We use a similar method as described in Appendix B to estimate the uncertainty of height above flotation, (Eq. 2), repeated here for convenience:

$$\mathbf{z_f} = (\mathbf{H_f} - \mathbf{H_a}) * (\frac{\rho_{sw} - \rho}{\rho_{sw}}), \tag{C1}$$

Flotation ice thickness, $\mathbf{H_f}$, as calculated from ICESat-2 measurements of surface elevation, has an error of $\sigma \mathrm{H}_{\mathrm{IS2}} = 4.2$ m (Appendix B). The BedMachine ice thickness product provides an area wide mean error of $\sigma \mathrm{H_a} = 119.8$ m and $\sigma \mathrm{H_a} = 44.2$ m for grounded areas only. This yields a combined error for the first term on the right hand side of $\sigma \mathrm{H} = \sqrt{\sigma^2_{\mathrm{H_f}} + \sigma^2_{\mathrm{H_a}}} = 119.9$ m and 44.4 m, respectively. The error in the second term is treated as a constant multiplicator from which we derive $\sigma \mathrm{z_f} = 119.9\mathrm{m} * (1027 - 886/1027) = 16.5$ m a.f. over the entire area including floating ice shelves and $\sigma \mathrm{z_f} = 44.4\mathrm{m} * (1027 - 886/1027) = 6.1$ m a.f. for grounded areas only.

Acknowledgments
We appreciate field efforts by the rest of the TARSAN on-ice team, Bruce Wallin, Douglas Fox, and Dale Pomraning, and our mountaineers, Cecelia Mortensen, Blair Fyffe, and Kirah Solomon. The authors also thank the efforts of scientists, captain and crew on board of the RVIB Nathaniel B. Palmer, which made the oceanographic data collection possible during the cruise NBP22-02. We acknowledge the support of the University of Wisconsin-Madison Automatic Weather Station program for the data set, data display, and information (NSF: Grant 1924730), as well as SkySat and DigitalGlobe for providing high-resolution satellite imagery. This work is from the TARSAN project, a component of the International Thwaites Glacier Collaboration (ITGC), and has the contribution no. ITGC-075. Support from National Science Foundation (NSF: Grant 1929991) and Natural Environment Research Council (NERC: Grant NE/S006419/1). Logistics for field work were provided by the NSF U.S. Antarctic Program, Ken Borek and NERC British Antarctic Survey. Christian T. Wild also thanks Wolfgang Rack for providing access to the COMSOL Multiphysics finite-element software.

Author contributions

CTW led data analysis, modeling, and writing. TSD acquired and processed CTD/LADCP data and contributed to the discussion of warm water intrusion into the sub-ice-shelf cavity. KEA assisted in analysis of ICESat and ICESat-2 data, the accuracy assessment and discussion of the results. GCB contributed to the discussion of ice-dynamical changes and pinning point interaction. MT processed GPS data and assisted the calculation of basal melt rates. AM, RH, TAS, KJH and ECP assisted in data interpretation and design of the study. All authors conducted fieldwork on land or at sea, discussed the re-

sults, and approved the final paper. We thank the editor and our reviewers (after they have done an amazing job).

References

Alley, K. E., Scambos, T. A., Anderson, R. S., Rajaram, H., Pope, A., & Haran, T. M. (2018). Continent-wide estimates of antarctic strain rates from landsat 8-derived velocity grids. *Journal of Glaciology*, *64*(244), 321–332. doi: https://doi.org/10.1017/jog.2018.23

Alley, K. E., Wild, C. T., Luckman, A., Scambos, T. A., Truffer, M., Pettit, E. C., ... others (2021). Two decades of dynamic change and progressive destabilization on the thwaites eastern ice shelf. *The Cryosphere*, *15*(11), 5187–5203. doi: https://doi.org/10.5194/tc-15-5187-2021

Benn, D. I., Luckman, A., Åström, J. A., Crawford, A., Cornford, S. L., Bevan, S. L., ... others (2021). Rapid fragmentation of thwaites eastern ice shelf, west antarctica. *The Cryosphere Discussions*, 1–25. doi: https://doi.org/10.5194/tc-2021-288

Berger, S., Drews, R., Helm, V., Sun, S., & Pattyn, F. (2017). Detecting high spatial variability of ice shelf basal mass balance, roi baudouin ice shelf, antarctica. *The Cryosphere*, *11*(6), 2675–2690. doi: https://doi.org/10.5194/tc-11-2675-2017

Bindschadler, R., Vornberger, P., Fleming, A., Fox, A., Mullins, J., Binnie, D., ... Gorodetzky, D. (2008). The landsat image mosaic of antarctica. *Remote Sens. Environ.*, *112*(12), 4214–4226. doi: 10.1016/j.rse.2008.07.006

Brunt, K. M., Fricker, H. A., Padman, L., Scambos, T. A., & O'Neel, S. (2010). Mapping the grounding zone of the ross ice shelf, antarctica, using icesat laser altimetry. *Annals of Glaciology*, *51*(55), 71–79. doi: https://doi.org/10.3189/172756410791392790

Brunt, K. M., Neumann, T. A., & Smith, B. E. (2019). Assessment of icesat-2 ice sheet surface heights, based on comparisons over the interior of the antarctic ice sheet. *Geophys. Res. Lett.*, *46*(22), 13072–13078. doi: https://doi.org/10.1029/2019gl084886

Chen, G. (1998). *Gps kinematic positioning for the airborne laser altimetry at long valley, california* (Unpublished doctoral dissertation). Massachusetts Institute of Technology.

Dotto, T. S., Naveira Garabato, A. C., Wåhlin, A. K., Bacon, S., Holland, P. R., Kimura, S., ... Jenkins, A. (2020). Control of the oceanic heat content of the getz-dotson trough, antarctica, by the amundsen sea low. *Journal of Geophysical Research: Oceans*, *125*(8), e2020JC016113. doi: https://doi.org/10.1029/2020JC016113

Dutrieux, P., Christianson, K. A., Lee, C., Rainville, L., Girton, J. B., Kim, T. W., & Lee, S. (2018). Seaglider and float observations beneath dotson ice shelf, west antarctica. In *American geophysical union, fall meeting 2018, abstract c11a-01.* Retrieved from `https://ui.adsabs.harvard.edu/abs/2018AGUFM.C11A..01D/abstract`

Dutrieux, P., Vaughan, D. G., Corr, H. F., Jenkins, A., Holland, P. R., Joughin, I., & Fleming, A. (2013). Pine island glacier ice shelf melt distributed at kilometre scales. *The Cryosphere*, *7*(5), 1543–1555. doi: https://doi.org/10.5194/tc-7-1543-2013

Egbert, G. D., & Erofeeva, S. Y. (2002). Efficient inverse modeling of barotropic ocean tides. *J. Atmos. Ocean. Technol.*, *19*(2), 183–204. doi: https://doi.org/10.1175/1520-0426(2002)019⟨0183:EIMOBO⟩2.0.CO;2

Favier, L., Gagliardini, O., Durand, G., & Zwinger, T. (2012). A three-dimensional full stokes model of the grounding line dynamics: effect of a pinning point beneath the ice shelf. *The Cryosphere*, *6*(1), 101–112. doi:

https://doi.org/10.5194/tc-6-101-2012

Favier, L., & Pattyn, F. (2015). Antarctic ice rise formation, evolution, and stability. *Geophysical Research Letters*, *42*(11), 4456–4463. doi: https://doi.org/10.1002/2015GL064195

Favier, L., Pattyn, F., Berger, S., & Drews, R. (2016). Dynamic influence of pinning points on marine ice-sheet stability: a numerical study in dronning maud land, east antarctica. *The Cryosphere*, *10*(6), 2623–2635. doi: https://doi.org/10.5194/tc-10-2623-2016

Förste, C., Bruinsma, S., Abrikosov, O., Flechtner, F., Marty, J. C., Lemoine, J. M., … Biancale, R. (2014). Eigen-6c4: The latest combined global gravity field model including goce data up to degree and order 2190 of gfz potsdam and grgs toulouse, paper presented at 5th goce user workshop, paris, 25–28 nov..

Fricker, H. A., Coleman, R., Padman, L., Scambos, T. A., Bohlander, J., & Brunt, K. M. (2009). Mapping the grounding zone of the amery ice shelf, east antarctica using insar, modis and icesat. *Antarctic Science*, *21*(5), 515–532. doi: https://doi.org/10.1017/S095410200999023X

Gardner, A. S., Fahnestock, M. A., & Scambos, T. A. (2019). [october 18, 2020]: Its_live regional glacier and ice sheet surface velocities [dataset]. data archived at national snow and ice data center.
doi: https://doi.org/10.5067/6II6VW8LLWJ7

Gardner, A. S., Moholdt, G., Scambos, T. A., Fahnstock, M., Ligtenberg, S., Van Den Broeke, M., & Nilsson, J. (2018). Increased west antarctic and unchanged east antarctic ice discharge over the last 7 years. *The Cryosphere*, *12*(2), 521–547. doi: https://doi.org/10.5194/tc-12-521-2018

Goldberg, D., Holland, D., & Schoof, C. (2009). Grounding line movement and ice shelf buttressing in marine ice sheets. *Journal of Geophysical Research: Earth Surface*, *114*(F4). doi: https://doi.org/10.1029/2008JF001227

Gourmelen, N., Goldberg, D. N., Snow, K., Henley, S. F., Bingham, R. G., Kimura, S., … others (2017). Channelized melting drives thinning under a rapidly melting antarctic ice shelf. *Geophysical Research Letters*, *44*(19), 9796–9804. doi: https://doi.org/10.1002/2017GL074929

Gudmundsson, G. (2011). Ice-stream response to ocean tides and the form of the basal sliding law. *The Cryosphere*, *5*(1), 259–270. doi: https://doi.org/10.5194/tc-5-259-2011

Gudmundsson, G. (2013). Ice-shelf buttressing and the stability of marine ice sheets. *The Cryosphere*, *7*(2), 647–655. doi: https://doi.org/10.5194/tc-7-647-2013

Han, H., & Lee, H. (2014). Tide deflection of campbell glacier tongue, antarctica, analyzed by double-differential sar interferometry and finite element method. *Remote Sens. Environ.*, *141*, 201-213. Retrieved from `https://www.sciencedirect.com/science/article/pii/S0034425713004082` doi: https://doi.org/10.1016/j.rse.2013.11.002

Holland, P. R., Bracegirdle, T. J., Dutrieux, P., Jenkins, A., & Steig, E. J. (2019). West antarctic ice loss influenced by internal climate variability and anthropogenic forcing. *Nature Geoscience*, *12*(9), 718–724. doi: https://doi.org/10.1038/s41561-019-0420-9

Howat, I. M., Porter, C., Smith, B. E., Noh, M. J., & Morin, P. (2019). The reference elevation model of antarctica. *The Cryosphere*, *13*(2), 665–674. doi: https://doi.org/10.5194/tc-13-665-2019

Jacobs, S. S., Jenkins, A., Giulivi, C. F., & Dutrieux, P. (2011). Stronger ocean circulation and increased melting under pine island glacier ice shelf. *Nature Geoscience*, *4*(8), 519–523. doi: https://doi.org/10.1038/ngeo1188

Jenkins, A., & Doake, C. S. M. (1991). Ice-ocean interaction on ronne ice shelf, antarctica. *J. Geophys. Res. Oceans*, *96*(C1), 791–813. doi: https://doi.org/10.1029/90jc01952

Jenkins, A., Shoosmith, D., Dutrieux, P., Jacobs, S., Kim, T. W., Lee, S. H., ... Stammerjohn, S. (2018). West antarctic ice sheet retreat in the amundsen sea driven by decadal oceanic variability. *Nature Geoscience*, *11*(10), 733–738. doi: https://doi.org/10.1038/s41561-018-0207-4

Khazendar, A., Rignot, E., Schroeder, D. M., Seroussi, H., Schodlok, M. P., Scheuchl, B., ... Velicogna, I. (2016). Rapid submarine ice melting in the grounding zones of ice shelves in west antarctica. *Nature communications*, *7*(1), 1–8. doi: https://doi.org/10.1038/ncomms13243

Kim, T.-W., Ha, H. K., Wåhlin, A., Lee, S., Kim, C.-S., Lee, J. H., & Cho, Y.-K. (2017). Is ekman pumping responsible for the seasonal variation of warm circumpolar deep water in the amundsen sea? *Continental Shelf Research*, *132*, 38–48. doi: https://doi.org/10.1016/j.csr.2016.09.005

Lenaerts, J. T., Ligtenberg, S. R., Medley, B., Van de Berg, W. J., Konrad, H., Nicolas, J. P., ... others (2018). Climate and surface mass balance of coastal west antarctica resolved by regional climate modelling. *Annals of Glaciology*, *59*(76pt1), 29–41. doi: https://doi.org/10.1017/aog.2017.42

Lilien, D. A., Joughin, I., Smith, B., & Gourmelen, N. (2019). Melt at grounding line controls observed and future retreat of smith, pope, and kohler glaciers. *The Cryosphere*, *13*(11), 2817–2834. doi: https://doi.org/10.5194/tc-13-2817-2019

Lilien, D. A., Joughin, I., Smith, B., & Shean, D. E. (2018). Changes in flow of crosson and dotson ice shelves, west antarctica, in response to elevated melt. *The Cryosphere*, *12*(4), 1415–1431. doi: https://doi.org/10.5194/tc-12-1415-2018

Love, A. E. H. (1906). *A treatise on the mathematical theory of elasticity.* Cambridge University Press, London.

Lucchitta, B. K., Mullins, K. F., Smith, C., & Ferrigno, J. G. (1994). Velocities of the smith glacier ice tongue and dotson ice shelf, walgreen coast, marie byrd land, west antarctica. *Annals of Glaciology*, *20*, 101–109. doi: https://doi.org/10.3189/1994AoG20-1-101-109

Matsuoka, K., Hindmarsh, R. C. A., Moholdt, G., Bentley, M. J., Pritchard, H. D., Brown, J., ... others (2015). Antarctic ice rises and rumples: Their properties and significance for ice-sheet dynamics and evolution. *Earth-Sci. Rev.*, *150*, 724–745. doi: https://doi.org/10.1016/j.earscirev.2015.09.004

McDougall, T. J., & Barker, P. M. (2011). Getting started with teos-10 and the gibbs seawater (gsw) oceanographic toolbox. *Scor/Iapso WG*, *127*, 1–28.

Milillo, P. (2021). Dataset for: Fast retreat of pope, smith, and kohler glaciers in west antarctica observed by satellite interferometry [dataset], dryad,. doi: https://doi.org/10.7280/D1B114

Milillo, P., Rignot, E., Rizzoli, P., Scheuchl, B., Mouginot, J., Bueso-Bello, J. L., ... Dini, L. (2022). Rapid glacier retreat rates observed in west antarctica. *Nature Geoscience*, *15*(1), 48–53. doi: https://doi.org/10.1038/s41561-021-00877-z

Moholdt, G., Padman, L., & Fricker, H. A. (2014). Basal mass budget of ross and filchner-ronne ice shelves, antarctica, derived from lagrangian analysis of icesat altimetry. *Journal of Geophysical Research: Earth Surface*, *119*(11), 2361–2380.

Morlighem, M. (2020). Measures bedmachine antarctica, version 2 [dataset]. boulder,colorado usa. nasa national snow and ice data center distributed active archive center. doi: https://doi.org/10.5067/E1QL9HFQ7A8M

Morlighem, M., Rignot, E., Binder, T., Blankenship, D., Drews, R., Eagles, G., ... others (2020). Deep glacial troughs and stabilizing ridges unveiled beneath the margins of the antarctic ice sheet. *Nature Geoscience*, *13*(2), 132–137. doi: https://doi.org/10.1038/s41561-019-0510-8

Mouginot, J., Rignot, E., & Scheuchl, B. (2014). Sustained increase in ice discharge from the amundsen sea embayment, west antarctica, from 1973 to 2013. *Geophysical Research Letters*, *41*(5), 1576–1584. doi: ttps://doi.org/10.1002/2013GL059069

Mueller, R., Padman, L., Dinniman, M. S., Erofeeva, S., Fricker, H. A., & King, M. (2012). Impact of tide-topography interactions on basal melting of larsen c ice shelf, antarctica. *Journal of Geophysical Research: Oceans*, *117*(C5). doi: https://doi.org/10.1029/2011JC007263

Padman, L., Erofeeva, S., & Joughin, I. (2003). Tides of the ross sea and ross ice shelf cavity. *Antarctic Science*, *15*(1), 31–40. doi: https://doi.org/10.1017/S0954102003001032

Padman, L., Erofeeva, S. Y., & Fricker, H. A. (2008). Improving antarctic tide models by assimilation of icesat laser altimetry over ice shelves. *Geophys. Res. Lett.*, *35*(22). doi: https://doi.org/10.1029/2008GL035592

Padman, L., Fricker, H. A., Coleman, R., Howard, S., & Erofeeva, L. (2002). A new tide model for the antarctic ice shelves and seas. *Annals of Glaciology*, *34*, 247–254. doi: https://doi.org/10.3189/172756402781817752

Paolo, F. S., Fricker, H. A., & Padman, L. (2015). Volume loss from antarctic ice shelves is accelerating. *Science*, *348*(6232), 327–331. doi: https://doi.org/10.1126/science.aaa0940

Rack, W., & Rott, H. (2004). Pattern of retreat and disintegration of the larsen b ice shelf, antarctic peninsula. *Annals of glaciology*, *39*, 505–510. doi: https://doi.org/10.3189/172756404781814005

Randall-Goodwin, E., Meredith, M., Jenkins, A., Yager, P., Sherrell, R., Abrahamsen, E. P., … others (2015). Freshwater distributions and water mass structure in the amundsen sea polynya region, antarcticafreshwater distributions and water mass structure in the asp region. *Elementa: Science of the Anthropocene*, *3*. doi: https://doi.org/10.12952/journal.elementa.000065

Reese, R., Gudmundsson, G. H., Levermann, A., & Winkelmann, R. (2018). The far reach of ice-shelf thinning in antarctica. *Nature Climate Change*, *8*(1), 53–57. doi: https://doi.org/10.1038/s41558-017-0020-x

Rignot, E., Jacobs, S., Mouginot, J., & Scheuchl, B. (2013). Ice-shelf melting around antarctica. *Science*, *341*(6143), 266–270. doi: https://doi.org/10.1126/science.1235798

Rignot, E., Mouginot, J., & Scheuchl, B. (2014). Measures insar-based ice velocity of the amundsen sea embayment, antarctica, version 1 [dataset]. boulder, colorado usa. nasa national snow and ice data center distributed active archive center. doi: https://doi.org/10.5067/MEASURES/CRYOSPHERE/nsidc-0545.001

Rignot, E., Mouginot, J., & Scheuchl, B. (2017). Measures insar-based antarctica ice velocity map, version 2 [dataset]. boulder, colorado usa. nasa national snow and ice data center distributed active archive center. doi: https://doi.org/10.5067/D7GK8F5J8M8R

Rignot, E., Mouginot, J., Scheuchl, B., Van Den Broeke, M., Van Wessem, M. J., & Morlighem, M. (2019). Four decades of antarctic ice sheet mass balance from 1979–2017. *Proceedings of the National Academy of Sciences*, *116*(4), 1095–1103. doi: https://doi.org/10.1073/pnas.1812883116

Scambos, T. A., Bohlander, J., Shuman, C. A., & Skvarca, P. (2004). Glacier acceleration and thinning after ice shelf collapse in the larsen b embayment, antarctica. *Geophysical Research Letters*, *31*(18). doi: https://doi.org/10.1029/2004GL020670

Scambos, T. A., White, T., Wallin, B., Collao-Barrios, G., Kratt, C., Tyler, S., … Ross, R. (in prep.). An ice-ocean-atmosphere multi-sensor system for polar research: Amigos-iii. *Journal of Glaciology: Instruments and Methods*.

Scheuchl, B., Mouginot, J., Rignot, E., Morlighem, M., & Khazendar, A. (2016). Grounding line retreat of pope, smith, and kohler glaciers, west antarctica, measured with sentinel-1a radar interferometry data. *Geophysical Research Letters*, *43*(16), 8572–8579. doi: https://doi.org/10.1002/2016GL069287

Schoof, C. (2007). Ice sheet grounding line dynamics: Steady states, stability, and hysteresis. *Journal of Geophysical Research: Earth Surface*, *112*(F3). doi: https://doi.org/10.1029/2006JF000664

Shean, D. E., Christianson, K., Larson, K. M., Ligtenberg, S. R., Joughin, I. R., Smith, B. E., ... Holland, D. M. (2017). Gps-derived estimates of surface mass balance and ocean-induced basal melt for pine island glacier ice shelf, antarctica. *The Cryosphere*, *11*(6), 2655–2674. doi: https://doi.org/10.5194/tc-11-2655-2017

Shean, D. E., Joughin, I. R., Dutrieux, P., Smith, B. E., & Berthier, E. (2019). Ice shelf basal melt rates from a high-resolution digital elevation model (dem) record for pine island glacier, antarctica. *The Cryosphere*, *13*(10), 2633–2656. doi: https://doi.org/10.5194/tc-13-2633-2019

Smith, B., Fricker, H. A., Gardner, A. S., Medley, B., Nilsson, J., Paolo, F. S., ... others (2020). Pervasive ice sheet mass loss reflects competing ocean and atmosphere processes. *Science*, *368*(6496), 1239–1242. doi: https://doi.org/10.1126/science.aaz5845

Smith, B., Fricker, H. A., Holschuh, N., Gardner, A. S., Adusumilli, S., Brunt, K. M., ... others (2019). Land ice height-retrieval algorithm for nasa's icesat-2 photon-counting laser altimeter. *Remote Sensing of Environment*, *233*, 111352.

Thurnherr, A. M. (2018). *How to process ladcp data with the ldeo software (versions ix.7 – ix.13).* Retrieved from `https://www.ldeo.columbia.edu/~ant/LADCP.html`

Wåhlin, A., Kalén, O., Arneborg, L., Björk, G., Carvajal, G., Ha, H. K., ... Stranne, C. (2013). Variability of warm deep water inflow in a submarine trough on the amundsen sea shelf. *Journal of Physical Oceanography*, *43*(10), 2054–2070. doi: https://doi.org/10.1175/JPO-D-12-0157.1

Walker, R. T., Parizek, B. R., Alley, R. B., Anandakrishnan, S., Riverman, K. L., & Christianson, K. (2013). Ice-shelf tidal flexure and subglacial pressure variations. *Earth and Planetary Science Letters*, *361*, 422–428. doi: https://doi.org/10.1016/j.epsl.2012.11.008

Weertman, J. (1974). Stability of the junction of an ice sheet and an ice shelf. *Journal of Glaciology*, *13*(67), 3–11. doi: https://doi.org/10.3189/S0022143000023327

Wild, C. T., Alley, K. E., Muto, A., Truffer, M., Scambos, T. A., & Pettit, E. C. (2022). Weakening of the pinning point buttressing thwaites glacier, west antarctica. *The Cryosphere*, *16*(2), 397–417. doi: https://doi.org/10.5194/tc-16-397-2022

Yang, H. W., Kim, T.-W., Dutrieux, P., Wåhlin, A., Jenkins, A., Ha, H. K., ... others (2022). Seasonal variability of ocean circulation near the dotson ice shelf, antarctica. *Nature communications*, *13*(1), 1–11. doi: https://doi.org/10.1038/s41467-022-28751-5

Zwally, H. J., Schutz, R., Hancock, D., & Dimarzio, J. (2014). Glas/icesat l2 global antarctic and greenland ice sheet altimetry data (hdf5), version 34 [dataset] boulder, colorado usa. *NASA National Snow and Ice Data Center Distributed Active Archive Center*. doi: https://doi.org/10.5067/ICESAT/GLAS/DATA209

Supplementary Material: A tale of two ice shelves by Wild et al., 2022

Flight path over the Dotson-Crosson Ice Shelf System in January 2022, on top of a timely Sentinel-1 SAR image from 9 Jan 2022

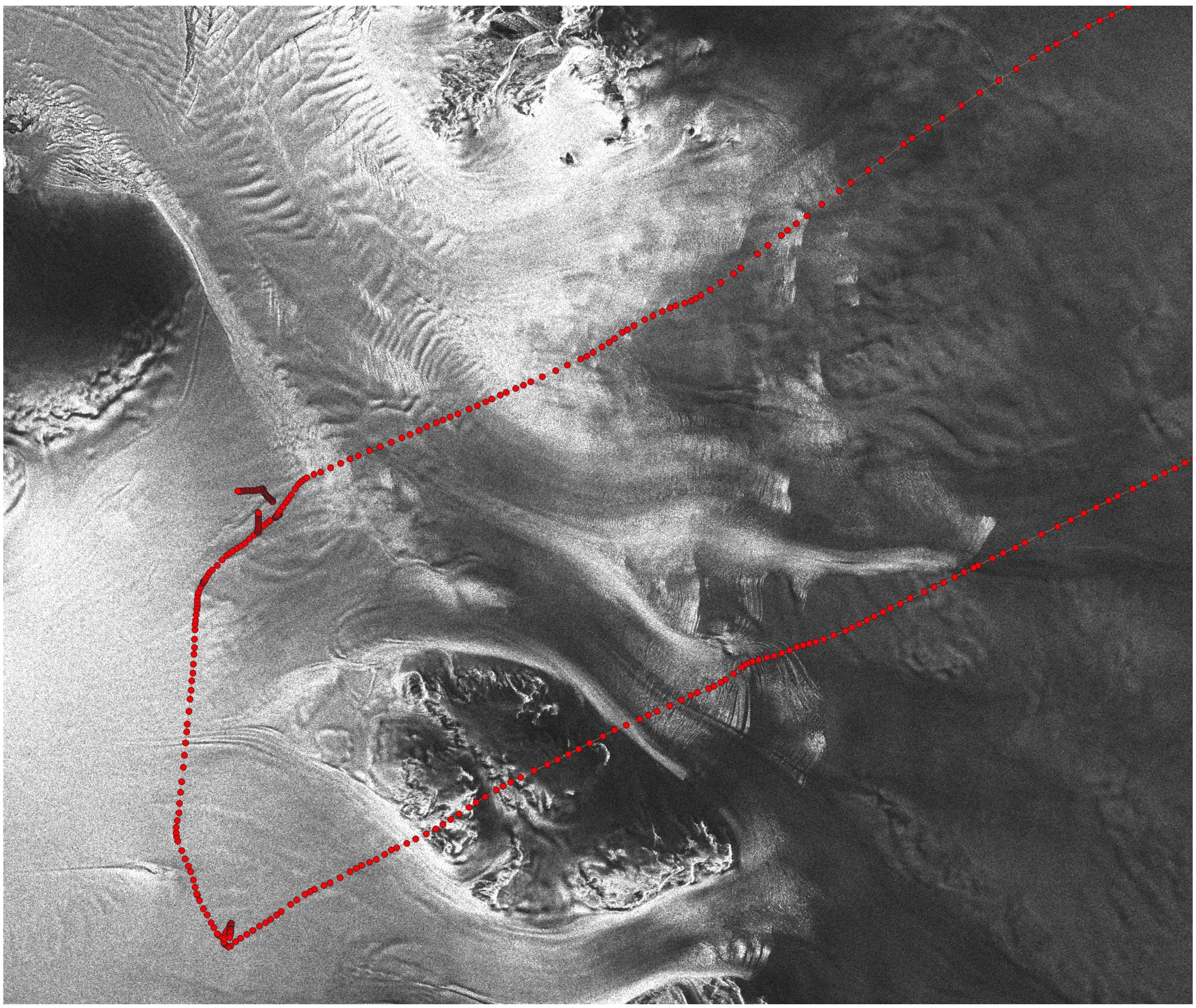

1) Surface crevassing on the Smith East Glacier (photo courtesy of Jesse Norquay)

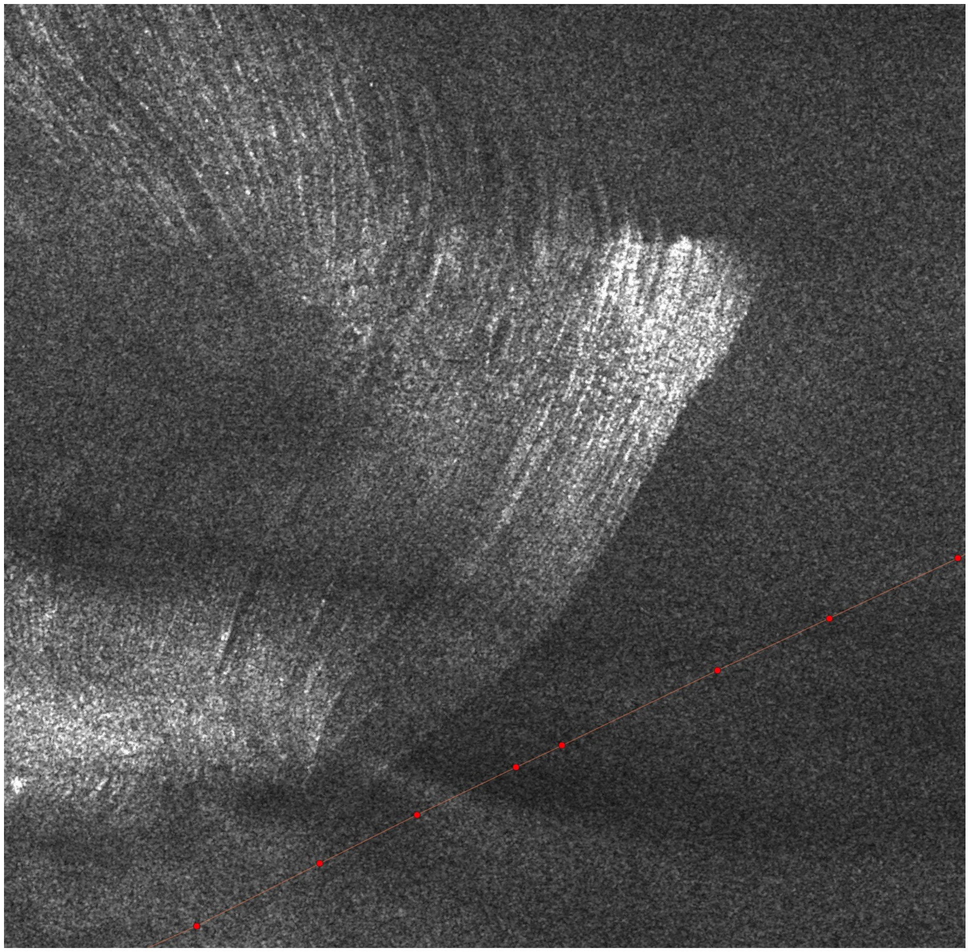

2) Surface crevassing between Smith East Glacier and Pope Glacier (photo courtesy of Jesse Norquay)

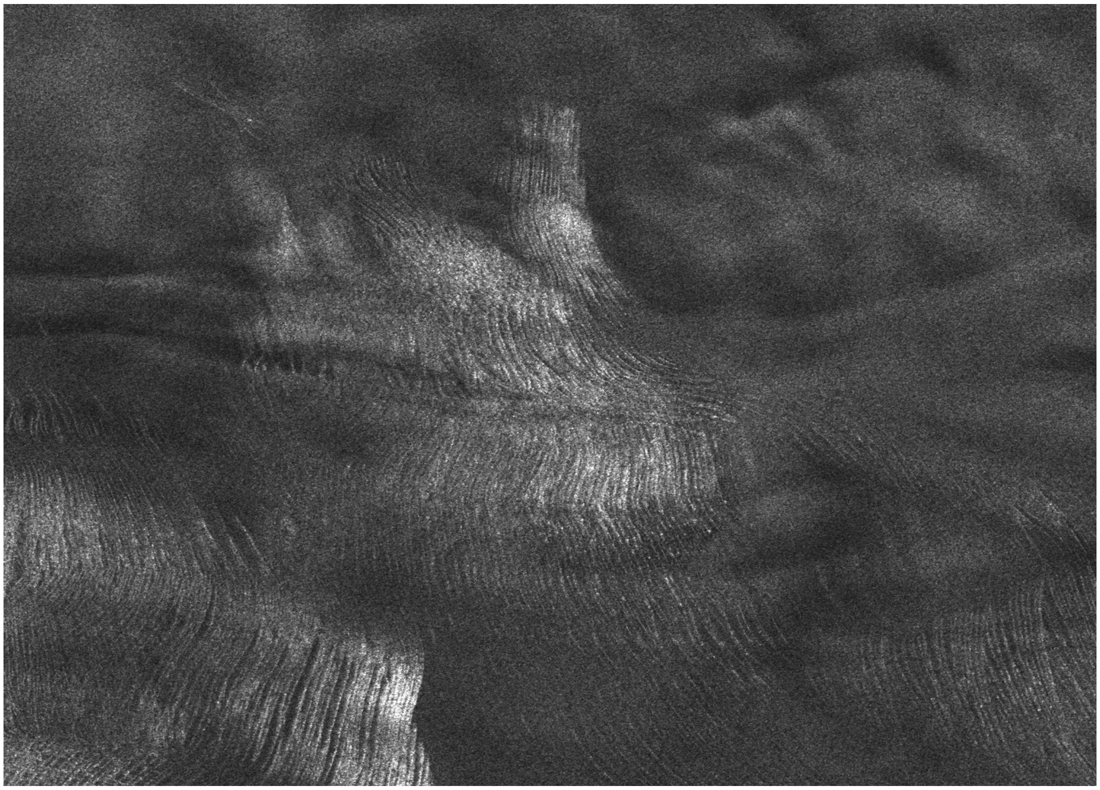

3) The new C7 pinning point near the grounding line of Smith West Glacier (photo courtesy of Jesse Norquay)

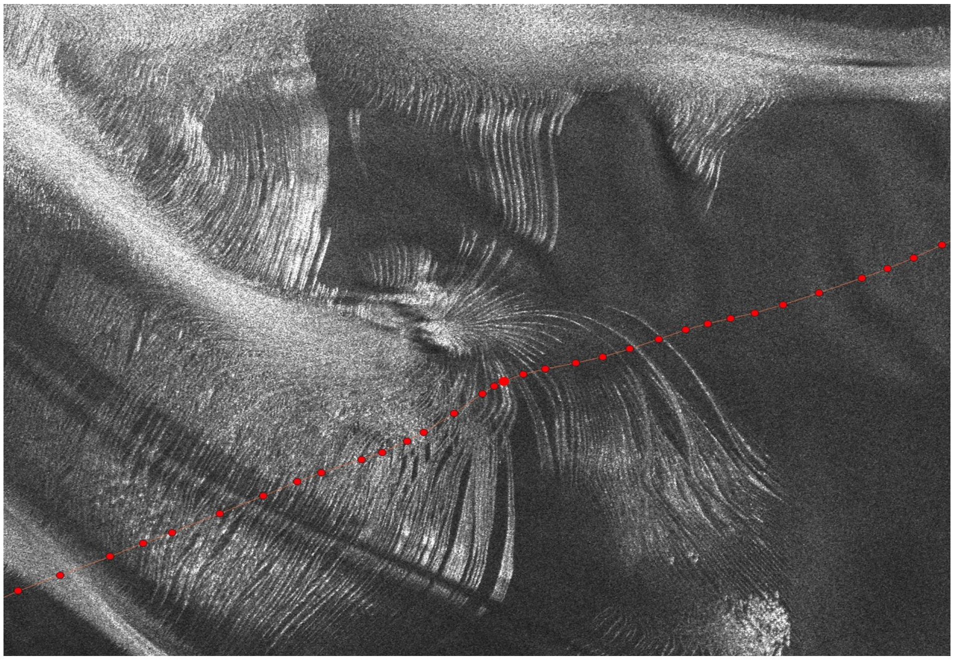

4) The D5 pinning point (Wunneberger Rock nunatak) in the Lower Dotson (photo courtesy of Jesse Norquay)

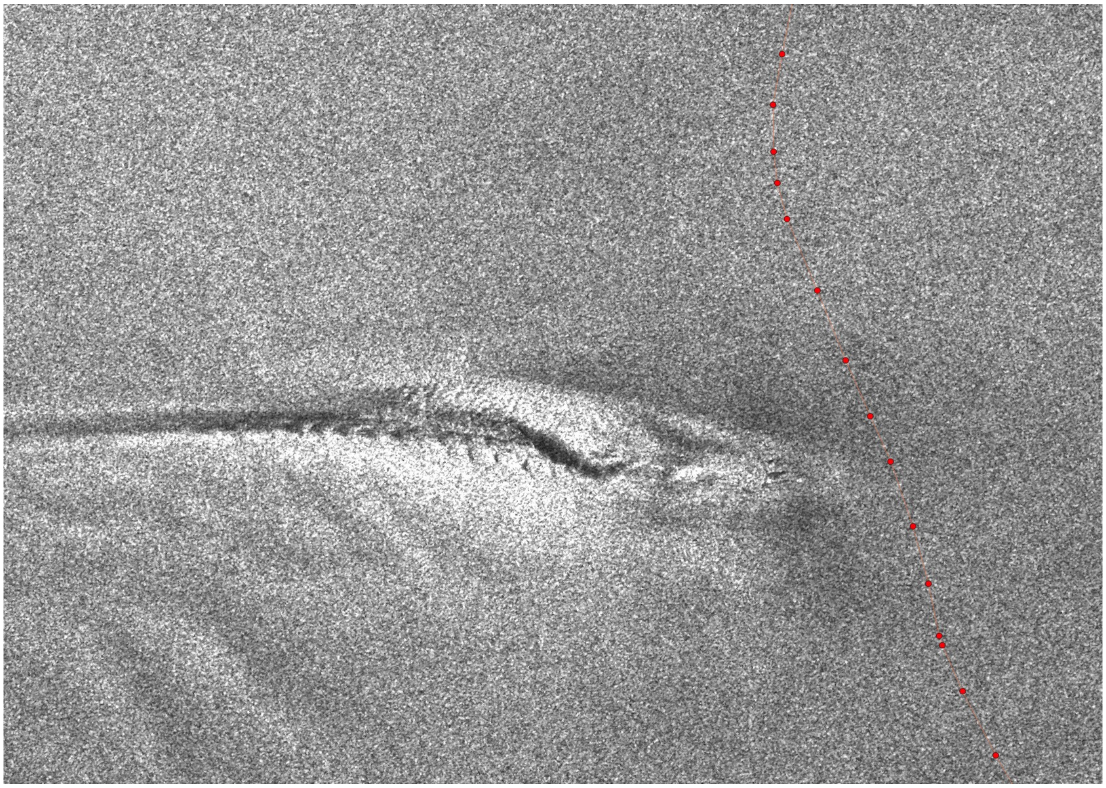

5) The D4 pinning point in the Upper Dotson (photo courtesy of Jesse Norquay)

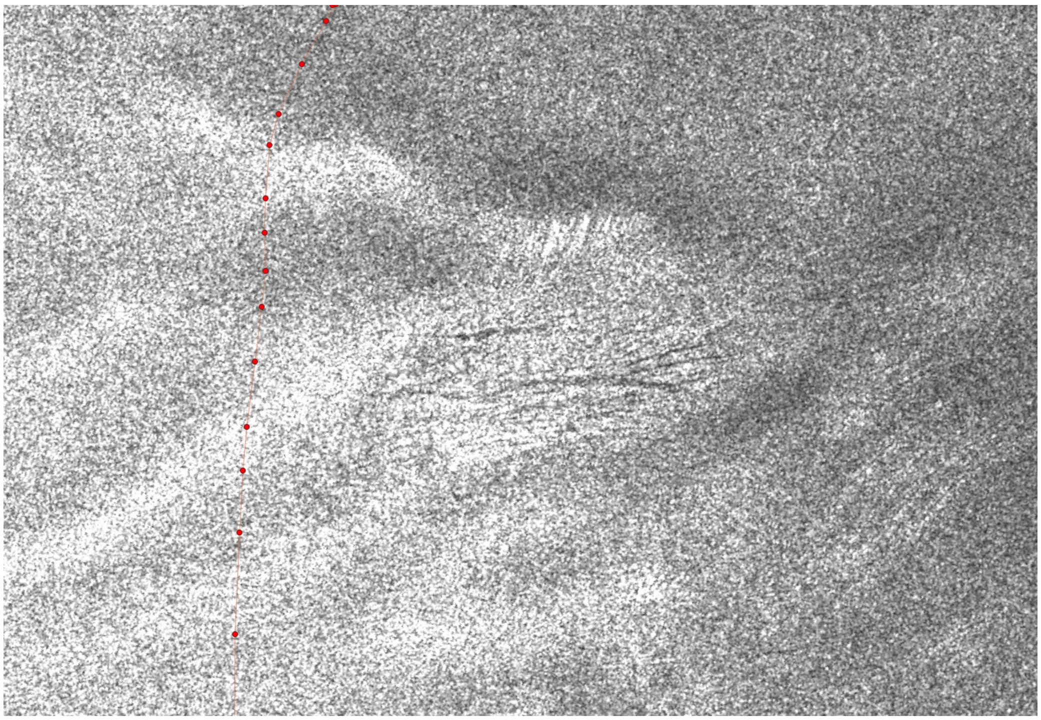

6) The D3 pinning point in the Upper Dotson (photo courtesy of Karen Alley)

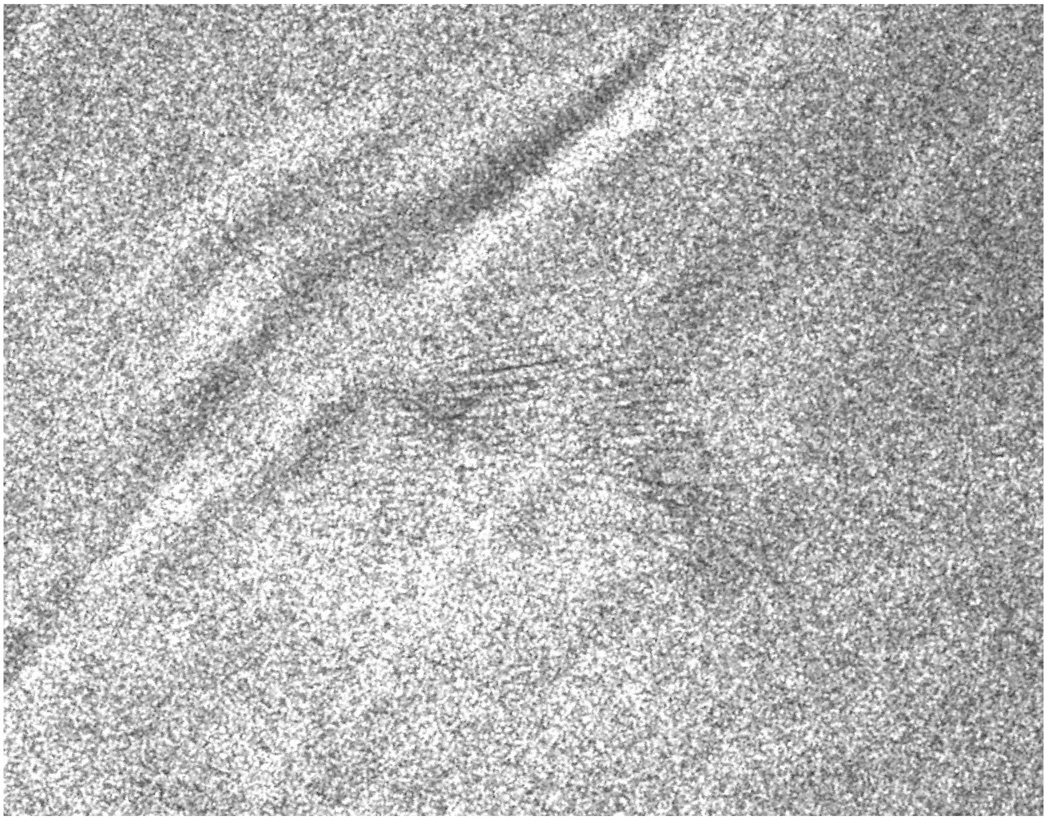

7) The C4 pinning point (photo courtesy of Karen Alley)

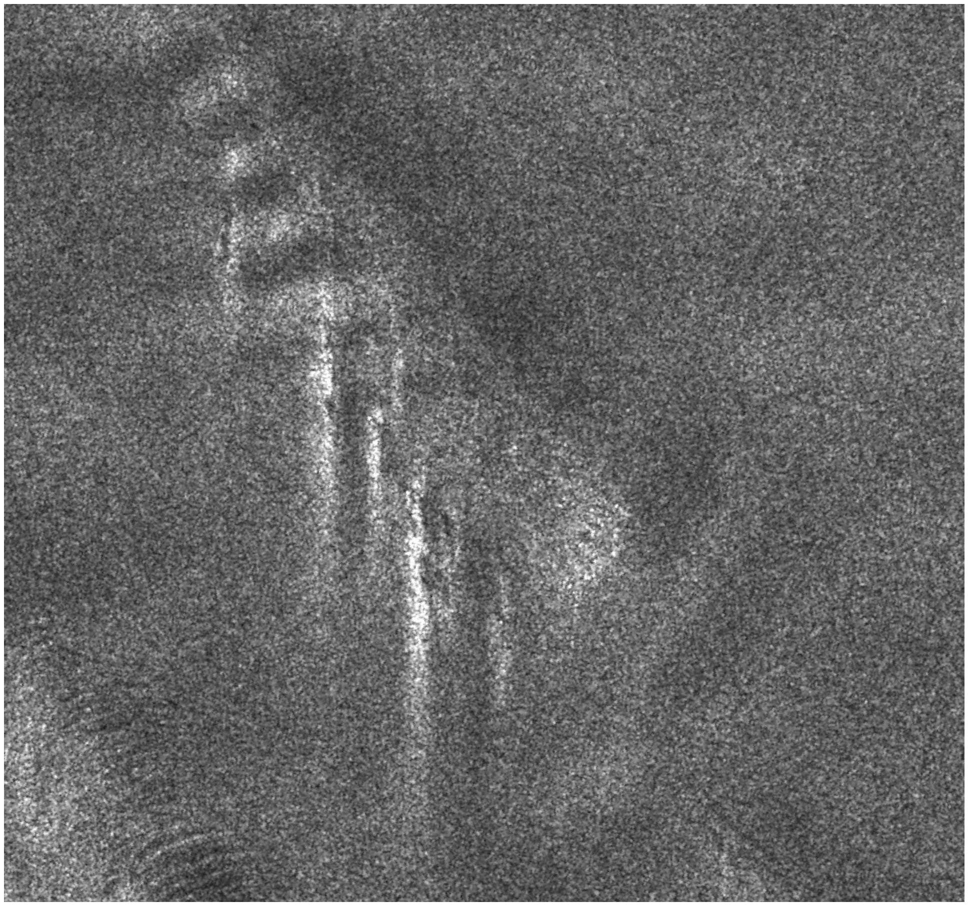

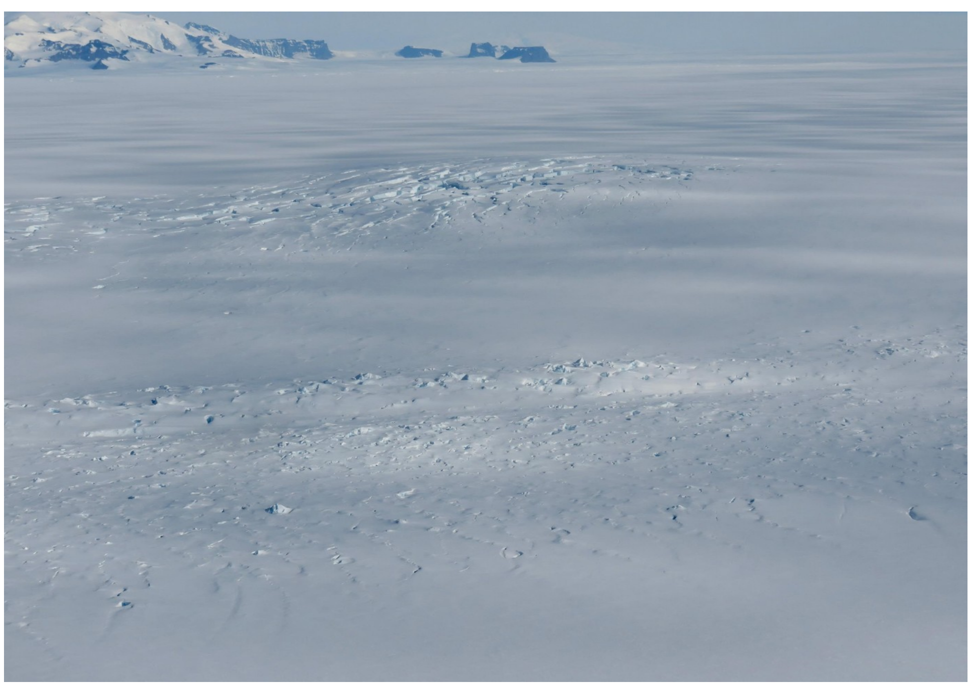

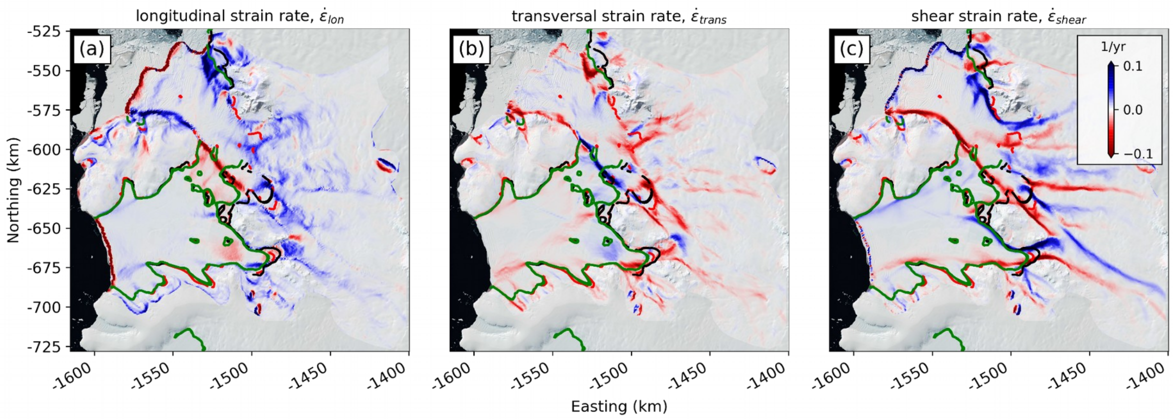

8) Figure of strain rate components used to calculate the dynamic thickness change

Figure S1: (a) longitudinal, (b) transversal and (c) shear strain rate components derived from MEaSUREs velocity components using the algorithm provided by Alley et al, 2018